

## AN X-RAY VIEW OF STAR FORMATION IN THE CENTRAL 3 KPC OF NGC 2403

MIHOKO YUKITA<sup>1</sup>, DOUGLAS A. SWARTZ<sup>2</sup>, ALLYN F. TENNANT<sup>3</sup>, AND ROBERTO SORIA<sup>4</sup>

*Submitted to Astronomical Journal*

### ABSTRACT

Archival *Chandra* observations are used to study the X-ray emission associated with star formation in the central region of the nearby SAB(s)cd galaxy NGC 2403. The distribution of X-ray emission is compared to the morphology visible at other wavelengths using complementary *Spitzer*, *GALEX*, and ground-based H $\alpha$  imagery. In general, the brightest extended X-ray emission is associated with HII regions and to other star-forming structures but is more pervasive; existing also in regions devoid of strong H $\alpha$  and UV emission. This X-ray emission has the spectral properties of diffuse hot gas ( $kT \sim 0.2$  keV) whose likely origin is in gas shock-heated by stellar winds and supernovae with  $\lesssim 20\%$  coming from faint unresolved X-ray point sources. This hot gas may be slowly-cooling extra-planar remnants of past outflow events, or a disk component that either lingers after local star formation activity has ended or that has vented from active star-forming regions into a porous interstellar medium.

*Subject headings:* galaxies: individual (NGC 2403) — galaxies: nuclei — galaxies: evolution — X-rays: galaxies

### 1. INTRODUCTION

Whether merger-induced collapse (Barnes & Hernquist 1992; Cole et al. 2000), bar-driven inflow (Kormendy & Kennicutt 2004), or dynamical friction (Noguchi 2000) builds structure at the center of a particular galaxy, it is likely that star formation and (if present) central black hole growth will be strongly regulated by feedback from massive stars (and AGN activity).

Since much of the current central massive object growth and star formation is occurring in small, low-density, disk-dominated spirals rather than the massive but fuel-starved ellipticals (Heckman et al. 2004), nearby late-type galaxies are the ideal laboratories to view the growth of galactic structure in the current epoch. Here, we investigate star formation, feedback, and the growth of the central region of NGC 2403. We focus on the unique perspective enabled by X-rays in viewing the violent and inherently high-energy phenomena associated with these dynamical processes and compare X-ray behavior to that exhibited at other wavelengths.

NGC 2403 is a SAB(s)cd galaxy in the M81 group of galaxies ( $D = 3.2$  Mpc,  $l' = 1$  kpc, Madore & Freedman 1991). It is the most massive,  $\sim 10^{10} M_{\odot}$ , galaxy in the second largest of three M81 subgroups. There are 7 dSph and dIrr satellites of NGC 2403 known within this subgroup (Karachentsev et al. 2002) ranging in size from  $\sim 3 \times 10^7$  to  $\sim 3 \times 10^9 M_{\odot}$  (Karachentsev et al. 2004).

As with many disk-dominated late-type spirals, NGC 2403 lacks a central bulge (Kent 1987) but does host a luminous compact nuclear star cluster first identified in IR images (Davidge & Courteau 2002). The mass

and luminosity of this cluster are comparable to those found in many late-type spirals (Böker et al. 2002) but it is older and less compact than typical for late-type galaxies (Yukita et al. 2007). The dominant age of stars within the nuclear star cluster is  $\sim 1.4$  Gyr (Yukita et al. 2007). There are numerous younger asymptotic giant branch, red, and early-type supergiants within the inner disk with stellar ages of 100 Myr (Davidge & Courteau 2002). Similarly, the H $\alpha$  surface brightness near the center is lower than in surrounding regions while the youngest ( $\sim 2$ – $10$  Myr) and most massive HII regions (Drissen et al. 1999) are 0.7 to 1.6 kpc from the center. Davidge & Courteau (2002) speculate that this age gradient may be due to the growth of a superbubble in the central region that has quenched star-formation in the central region while triggering activity further out through compression of surrounding gas during bubble expansion. In this picture, nuclear star formation may be an episodic phenomenon with roughly a few 100 Myr interval between major star-forming events.

Such a star formation cycle requires a replenishing source of cold gas. Sheth et al. (2005), using molecular gas maps, showed that bulges can be built by bar-driven gas inflow but that the process requires of order a Hubble time in galaxies like NGC 2403. Other studies have shown that the molecular and atomic gas in the central regions of NGC 2403 amount to only a small fraction of the dynamical mass (e.g., Thornley & Wilson 1995). Importantly, the central total gas surface density (e.g., Thornley & Wilson 1995; Martin & Kennicutt 2001), at least on kiloparsec spatial scales, is below the critical value for star formation (Kennicutt 1989) yet the global star-formation rate in NGC 2403 is a moderate  $1.2 M_{\odot} \text{ yr}^{-1}$ .

More pertinent to the current study are several independent investigations of the dynamics of the HI gas in NGC 2403 (Sicking 1997; Schaap et al. 2000; Fraternali et al. 2002b). The HI rotation curve shows a flat gravitational potential typical of late-type spirals but there is also slower-rotating neutral hydrogen ex-

<sup>1</sup> University of Alabama in Huntsville, Dept. of Physics, Huntsville, AL, USA

<sup>2</sup> Universities Space Research Association, NASA Marshall Space Flight Center, VP62, Huntsville, AL, USA

<sup>3</sup> Space Science Office, NASA Marshall Space Flight Center, VP62, Huntsville, AL, USA

<sup>4</sup> Mullard Space Science Laboratory, University College London, Holmbury St. Mary, Surrey RH5 6NT, UK

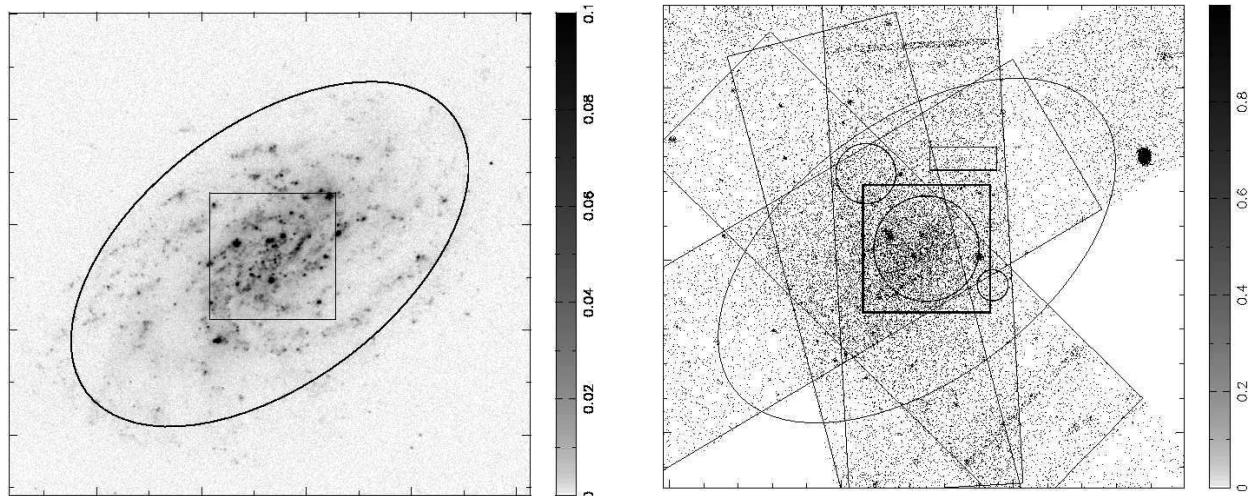


FIG. 1.— Left: The *GALEX* FUV image of NGC 2403. The  $21'.9 \times 12'.3$  ellipse makes  $D_{25}$  isophote of NGC 2403. The central  $6' \times 6'$  region is shown as a square. The gray scale indicates intensity level in the unit of  $\text{ct s}^{-1} \text{ pixel}^{-2}$ . One pixel corresponds to  $1''.5$ . Right: The same region in the merged X-ray data. The outer boundaries of the ACIS S2-S3-S4 combination are shown as thin-lined rectangles for each of the 4 overlaid observations. The central  $6' \times 6'$  region is shown as a thick-lined square. The large circle in the center is the  $2'.5$  radius circle used for the X-ray residual emission spectral analysis (see text). The two smaller circles and the small rectangle identify the background regions used for analysis of this residual emission. The gray scale indicates intensity levels in units of  $\text{ct pixel}^{-2}$ . One pixel corresponds to  $0''.492$ .

tending up to 15 kpc above the disk. Many properties of this anomalous HI gas can be explained as galactic fountains (Shapiro & Field 1976; Bregman 1980; Spitzer 1990) but an additional, external, source of cold gas such as infalling clouds or even small satellite galaxies might also be required (Fraternali & Binney 2006, 2008; Struck & Smith 2009). High-resolution VLA observations of NGC 2403 (Fraternali et al. 2002b) show very anomalous kinematic features on small scales that may be evidence of such clouds. Direct evidence of fountain activity is less conclusive. Measurements of  $H\alpha$  emission line widths at several locations across the galaxy (Fraternali et al. 2004) found only a few small-scale fountain-like features. To match the observed HI inflow with hot gas outflow would require many thousands of these small-scale fountains. Analysis of the spatial distribution of diffuse hot X-ray-emitting gas in NGC 2403 (Fraternali et al. 2002a) concluded that as little as a few percent or as much as the majority of the inflowing HI can be matched by outflowing diffuse hot gas, depending on assumptions made. Thus, it is not yet clear whether the buildup of the central regions of NGC 2403 is being fueled cyclically through galactic fountains, or by accreting gas from the intergalactic medium, or through mergers of small-scale gaseous satellites.

If galactic fountains are at work and are the source of the majority of the observed infalling HI gas, then there should be an imprint of this process in the X-ray emission from the disk correlated with the source of the fountains; namely localized star-forming regions that heat the gas through massive stars to the point of breakout from the disk.

We confine our study of NGC 2403 to the inner  $6' \times 6'$  nuclear region (corresponding to  $5.6 \times 5.6$  kpc; Figure 1 left panel). This region is small enough to be fully imaged within a single observation by most instruments used in this study yet includes a large portion of the actively

star-forming regions of NGC 2403 including 5 of the 6 giant HII regions identified by Drissen et al. (1999).

We begin (§ 2) with an independent analysis of the X-ray data; examining X-ray-detected discrete sources and the underlying residual X-ray emission. This analysis extends the previous work of Schlegel & Panuti (2003) and of Fraternali et al. (2002a) by including 3 subsequent *Chandra* observations which allow us to better quantify the spectral and temporal behavior of the X-ray emission. Our results are consistent with both these previous investigations. We expand our analysis to include optically-identified supernova remnants (SNRs) and HII regions. Although individually X-ray-faint, we are able to characterize their bulk (average) X-ray temperatures and other X-ray properties using stacking analysis.

We then turn to analysis of individual massive star-forming regions (§ 3) in an attempt to determine the X-ray emission properties of these regions as a function of their age, mass, and extinction properties. We use a combination of (ground-based)  $H\alpha$ , mid-IR (*Spitzer*), and UV (*GALEX*) images to define these regions and to determine their basic physical characteristics. We then use our knowledge of the differences in X-ray properties between HII regions and SNRs assembled in § 2 to interpret the properties of the hot gas.

## 2. *Chandra* X-RAY OBSERVATIONS AND PRELIMINARY ANALYSIS

In this section, archival *Chandra* images are examined to derive the X-ray properties of four different source populations in NGC 2403; namely, bright X-ray-detected sources (mainly luminous X-ray binaries and background AGNs), optically-identified SNRs, optically-identified HII regions, and the underlying unresolved X-ray emission. This allows us to parameterize these different types of sources in terms of their X-ray temperatures, luminosity distributions, and emission measures. This information will be used in § 3 to investigate in-

TABLE 1  
*Chandra* OBSERVATION LOG

Date	ObsID	Instruments & Mode	GTI
2001/04/17	2014	ACIS-S TE	36.1 ks
2004/08/13	4628	ACIS-S TE	47.1 ks
2004/10/03	4629	ACIS-S TE	45.1 ks
2004/12/22	4630	ACIS-S TE	50.6 ks

dividual massive star-forming regions defined at other wavelengths.

NGC 2403 was observed in full-frame mode with *Chandra* ACIS-S on four occasions for a total of  $\sim 180$  ks (Table 1). We obtained level 1 event lists for all four observations from the *Chandra* data archive<sup>5</sup> and reprocessed them using the CIAO (version 3.3.0.1) tool `acis_process_events` and calibration database CALDB 3.2.1. Reprocessing removed pixel randomization, applied CTI- and time-dependent gain corrections, and removed events with bad grades or bad status bits as well as bad and hot pixels. We created lightcurves for each observation using a 1 ks binning to check for periods of high background. We excluded intervals with total count rates  $> 3\sigma$  above the mean rate for each observation. The final Good Time Intervals for the observations are listed in Table 1.

SN 2004dj was used to define a common registration among the data sets. For this purpose, a circular Gaussian was fit to the image of the supernova to obtain an accurate centroid then the coordinates were adjusted to agree with the known position of SN 2004dj (J2000 R.A.= $7^h37^m17.044^s$ , Decl.= $+65^\circ35'57.84''$ , Argo et al. 2004). To register pre-supernova data, we bootstrapped using a bright point source near the aimpoint that is common to both pre- and post-supernova data. The four co-aligned *Chandra* data sets were combined using the FTOOL utility `fmerge` to form a fifth merged dataset. The right panel of Figure 1 displays the merged X-ray image. The longest cumulative exposure is near the center of the galaxy where we have selected a  $6' \times 6'$  region for analysis as indicated. Also shown are the galaxy's  $D_{25}$  ellipse, corresponding to the 25 mag-sec<sup>-2</sup> contour in  $B$ . The  $6' \times 6'$  region contains many point-like sources, extended star forming regions, and an extended region of X-ray emission near the galactic center. With the exception of the bright point-like X-ray sources, we are primarily concerned with the soft X-ray emission components of NGC 2403. For the soft emission, we fit spectra in the 0.4–2.0 keV range but quote results such as luminosities in the more familiar 0.5–2.0 keV band. For point sources, the fitting range is extended to higher X-ray energies.

### 2.1. X-ray Source and Region Definitions

The source-finding tool described by Tennant (2006) was applied to all five datasets to search for discrete X-ray sources. The search was limited to the central  $6' \times 6'$  region and to events within the full *Chandra* energy range 0.3–8.0 keV. Fifty-eight sources were detected in the merged dataset with a S/N above 2.8 and with a minimum of 5  $\sigma$  above background uncertainty (corresponding to a detection limit of about 8–10 counts for

<sup>5</sup> <http://cda.harvard.edu/chaser/>

TABLE 2  
X-RAY POINT SOURCES

R.A. J2000	Decl J2000	Count Rate <sup>a</sup> 10 <sup>-4</sup> cts s	$L_X$ <sup>b</sup> 10 <sup>36</sup> erg s <sup>-1</sup>	Variability
07 36 24.5	+65 37 13.1	1.2 ± 0.7	0.5 ± 0.3	
07 36 24.5	+65 37 34.9	-0.3 ± 0.4	-0.1 ± 0.1	
07 36 25.2	+65 38 40.6	7.9 ± 1.7	3.1 ± 0.7	S
07 36 25.6	+65 35 39.7	1158 ± 12	456.6 ± 4.7	L S
07 36 25.9	+65 37 57.0	0.1 ± 0.6	0.0 ± 0.2	
07 36 26.7	+65 36 20.9	0.8 ± 0.4	0.3 ± 0.2	
07 36 32.6	+65 34 52.6	0.9 ± 0.3	0.4 ± 0.1	
07 36 32.5	+65 38 20.0	0.1 ± 0.6	0.0 ± 0.2	
07 36 32.5	+65 39 00.7	29.7 ± 3.0	11.7 ± 1.2	S
07 36 33.0	+65 34 57.8	3.9 ± 0.6	1.6 ± 0.2	L S
07 36 34.0	+65 35 40.7	0.7 ± 0.3	0.3 ± 0.1	
07 36 34.1	+65 38 54.7	54.4 ± 3.9	21.4 ± 1.6	L
07 36 35.6	+65 36 08.4	3.1 ± 0.5	1.2 ± 0.2	
07 36 37.9	+65 38 15.7	2.0 ± 0.8	0.8 ± 0.3	
07 36 37.9	+65 37 37.2	1.2 ± 0.4	0.5 ± 0.2	
07 36 42.0	+65 36 51.8	52.6 ± 2.0	20.7 ± 0.8	
07 36 43.0	+65 37 09.7	0.7 ± 0.3	0.3 ± 0.1	
07 36 45.2	+65 35 57.3	3.1 ± 0.5	1.2 ± 0.2	
07 36 45.8	+65 36 40.5	2.4 ± 0.5	0.9 ± 0.2	
07 36 46.1	+65 36 13.6	-0.0 ± 0.1	-0.0 ± 0.1	L
07 36 46.8	+65 35 58.1	1.0 ± 0.3	0.4 ± 0.1	
07 36 47.5	+65 36 19.0	7.3 ± 0.8	2.9 ± 0.3	L S
07 36 47.6	+65 36 22.9	5.5 ± 0.7	2.1 ± 0.3	
07 36 50.1	+65 36 03.7	20.9 ± 1.3	8.2 ± 0.5	L
07 36 52.0	+65 36 41.0	2.5 ± 0.5	1.0 ± 0.2	
07 36 52.5	+65 36 46.0	0.9 ± 0.3	0.4 ± 0.1	
07 36 53.8	+65 33 32.1	0.9 ± 0.2	0.4 ± 0.1	
07 36 53.9	+65 35 35.2	0.5 ± 0.2	0.2 ± 0.1	
07 36 55.4	+65 36 08.3	2.5 ± 0.4	1.0 ± 0.1	
07 36 55.6	+65 35 40.9	436.8 ± 5.0	172.3 ± 2.0	L S
07 36 56.1	+65 37 15.6	2.4 ± 0.5	0.9 ± 0.2	
07 36 57.2	+65 36 03.7	2.8 ± 0.4	1.1 ± 0.2	
07 37 00.7	+65 36 06.2	1.1 ± 0.3	0.4 ± 0.1	
07 37 00.8	+65 34 17.9	14.2 ± 0.9	5.6 ± 0.4	L S
07 37 01.8	+65 38 27.2	-0.1 ± 0.2	-0.0 ± 0.1	
07 37 02.2	+65 34 45.8	0.4 ± 0.2	0.2 ± 0.1	
07 37 02.4	+65 36 01.5	1.2 ± 0.3	0.5 ± 0.1	
07 37 02.6	+65 37 10.8	2.4 ± 0.4	0.9 ± 0.1	
07 37 02.9	+65 34 37.9	1.4 ± 0.3	0.6 ± 0.1	
07 37 06.4	+65 34 51.9	0.7 ± 0.2	0.3 ± 0.1	
07 37 06.9	+65 36 21.7	0.7 ± 0.2	0.3 ± 0.1	
07 37 07.0	+65 36 14.1	1.1 ± 0.3	0.5 ± 0.1	
07 37 07.1	+65 35 56.6	2.1 ± 0.4	0.8 ± 0.1	
07 37 07.4	+65 34 55.9	21.1 ± 1.1	8.3 ± 0.4	L S
07 37 09.2	+65 35 44.2	23.8 ± 1.2	9.4 ± 0.5	L
07 37 09.4	+65 35 01.4	0.3 ± 0.2	0.1 ± 0.1	
07 37 09.6	+65 33 05.8	3.0 ± 0.4	1.2 ± 0.2	
07 37 09.9	+65 35 46.9	0.7 ± 0.2	0.3 ± 0.1	
07 37 10.2	+65 33 11.2	3.5 ± 0.5	1.4 ± 0.2	
07 37 11.3	+65 38 14.2	1.0 ± 0.3	0.4 ± 0.1	
07 37 11.6	+65 33 45.9	51.7 ± 1.7	20.4 ± 0.7	S
07 37 13.1	+65 35 58.2	3.0 ± 0.4	1.2 ± 0.2	
07 37 14.9	+65 34 29.0	23.7 ± 1.2	9.4 ± 0.5	S
07 37 16.1	+65 33 28.9	1.9 ± 0.3	0.8 ± 0.1	
07 37 17.1	+65 35 57.9	42.4 ± 1.6	16.7 ± 0.6	L S
07 37 17.6	+65 36 23.4	1.3 ± 0.3	0.5 ± 0.1	
07 37 17.9	+65 37 26.5	1.2 ± 0.3	0.5 ± 0.1	
07 37 18.0	+65 35 09.4	1.0 ± 0.3	0.4 ± 0.1	

NOTE. — Units of right ascension are hours, minutes, and seconds, and units of declination are degrees, arcminutes, and arcseconds.

<sup>a</sup> Count rates for ASIC-S3, taking the 0.5 – 2.0 keV energy band.

<sup>b</sup>  $L_X$  for the 0.5 – 2.0 keV energy band.  $L_X$  is computed using the bremsstrahlung model obtained from Table 3 (see text).

a typical on-axis source). This tally included all sources detected in the individual observations (provided they were within the FOV of the individual images) and all those previously reported by Schlegel & Pannuti (2003) within our  $6' \times 6'$  field. The X-ray point sources and their properties are listed in Table 2.

Since we are primarily interested in star-formation and the X-ray properties of recent and current star-forming events in this study, we also examined the X-ray emission from known SNRs and HII regions. For this purpose, we first masked out the X-ray-detected point-like sources in the field of the merged image using a mask radius equal to 3 times the half-width of a Gaussian approximation to the instrumental point spread function (PSF). Larger radii were used, as necessary, for a few bright sources with strong emission in their PSF wings. Spectral information was then extracted from events falling within the area defined by optically identified SNRs from [SII]/H $\alpha$  ratio by Matonick et al. (1997) using their listed locations and source radii. One arcsecond ( $\sim 16$  pc) radii are used for the SNRs whose sizes are unlisted. Local backgrounds were also extracted from surrounding annuli. There are 29 cataloged SNRs within our  $6' \times 6'$  field. There are also three candidate radio SNRs in our field (Pannuti et al. 2007). One (denoted  $\mu$  by Pannuti et al. 2007) is already included in the list of optically-identified SNRs. Another (denoted TH2 by Pannuti et al. 2007) is a strong X-ray source,  $L_X = 2 \times 10^{37}$  erg s $^{-1}$ , as previously noted by Pannuti et al. (2007). However, no radio spectral indices are available for any of these candidate radio SNRs. Therefore, we opt to omit TH2 from our list of candidate SNRs as it is anomalously bright if it is, in fact, a SNR. It remains classified as a discrete X-ray source in our tabulation.

A similar procedure was attempted using the HII regions defined by Sivan et al. (1990) based on photographic images but many of these cataloged objects did not correspond to HII regions visible in a recent continuum-subtracted H $\alpha$  CCD image. This is due mostly to crude modeling of the HII structure which resulted in poor estimates of source positions and sizes. Therefore, we constructed our own catalog of HII regions defined as circular approximations to the areas enclosed by surface brightness contours corresponding to a level of  $20\times$  the background in our continuum-subtracted H $\alpha$  image. There are 58 HII regions defined in this way within our  $6' \times 6'$  field including 5 of the 6 giant HII regions identified previously by Drissen et al. (1999).

There are four point-like sources detected by our source-finding trial that spatially coincide with SNRs. Two more detected sources lie within a bright extended HII region. Upon further examination, all these sources were determined to be steady thermal sources and were therefore assigned to the SNR (HII) category rather than to the general category of point sources for purposes of our analysis. Conversely, the PSF wings of bright point sources overlap with the positions of two of the cataloged SNRs. These two SNRs were therefore excluded from our analysis because of this contamination. The three historical supernovae, SN 2004dj (a strong X-ray source), SN 2002kg and SN 1954J (both fainter than our detection limit) and the X-ray-bright candidate radio SNR were also not considered further in this study.

Finally, we also examined the properties of the X-ray emission remaining after the X-ray point sources and the optically-identified SNRs and HII regions are excluded. This residual component is likely comprised of unresolved (faint) XRBs and other low-luminosity objects related to the stellar content of NGC 2403, extended diffuse hot gas

TABLE 3  
POINT SOURCES FITTING RESULTS

Fit Parameters	Bremsstrahlung	Powerlaw
$N_H$ ( $10^{21}$ cm $^{-2}$ )	$1.9^{+0.1}_{-0.1}$	$2.5^{+0.2}_{-0.2}$
$kT$ (keV)	$4.7^{+0.6}_{-0.5}$	
$\Gamma$		$1.87^{+0.06}_{-0.06}$
Normalization ( $10^{-4}$ )	$5.9^{+0.2}_{-0.2}$	$5.4^{+0.3}_{-0.3}$
$L_X(0.5-2.0$ keV)/ $10^{38}$ erg s $^{-1}$	$7.7^{+0.3}_{-0.4}$	$7.7^{+0.5}_{-0.5}$
$L_X(2.0-10$ keV)/ $10^{38}$ erg s $^{-1}$	$16.7^{+0.8}_{-1.1}$	$20.0^{+0.8}_{-0.8}$
$\chi^2/\text{dof}$	185/197	211/197

within the disk and halo of NGC 2403, and unresolved background (primarily AGN) and foreground (local diffuse Galactic) emission. Inspection of the residual emission image shows a clear excess above the background in the central regions of NGC 2403.

We examine the X-ray properties of these four source types in the following subsections.

## 2.2. Discrete X-ray-Detected Sources

Schlegel & Pannuti (2003) have already presented the properties of the discrete source population detected in the first *Chandra* observation of NGC 2403. Here, our interest is only in the average spectral shape of the discrete sources and their luminosity distribution. The average spectrum can be represented by co-adding the source spectra from only the first observation. This provides sufficient source counts for characterizing the spectrum yet avoids complications that arise when combining observations made at different times during the *Chandra* mission. The spectra of the individual point sources (and corresponding backgrounds) were co-added and weighted ancillary response (ARF) and response matrix (RMF) files were generated using CIAO tool *acis-spec*. The resulting spectrum was grouped to ensure at least 20 counts in each spectral bin. The source spectrum was modelled using the XSPEC spectral-fitting utility (version 11.3.2t).

We applied both absorbed powerlaw and bremsstrahlung models to the co-added discrete source spectrum. The fitting results are shown in Table 3, and the spectrum is shown in Figure 2. Although we are mainly interested in the energy range 0.5–2.0 keV, a more precise fit can be made by extending the spectral fits to at least 5 keV. Over this range, the best-fitting model is the thermal bremsstrahlung model. This model is used to estimate the luminosities of the individual sources. For this purpose, separate ARF and RMF files for each source and for each observation were created and used in the fit. The hydrogen column density and bremsstrahlung temperature were held fixed at the values from Table 3 during the fitting; only the model normalization was allowed to vary. The resulting 0.5–2.0 keV luminosities, averaged over the four observations, are listed in Table 2.

The flux estimates were used to check for variability of sources between and during individual *Chandra* observations. This check helps to differentiate between diffuse emission associated with star-formation that has a relatively soft X-ray spectrum and no variability and emission from XRBs that is spectrally hard and often variable over time.

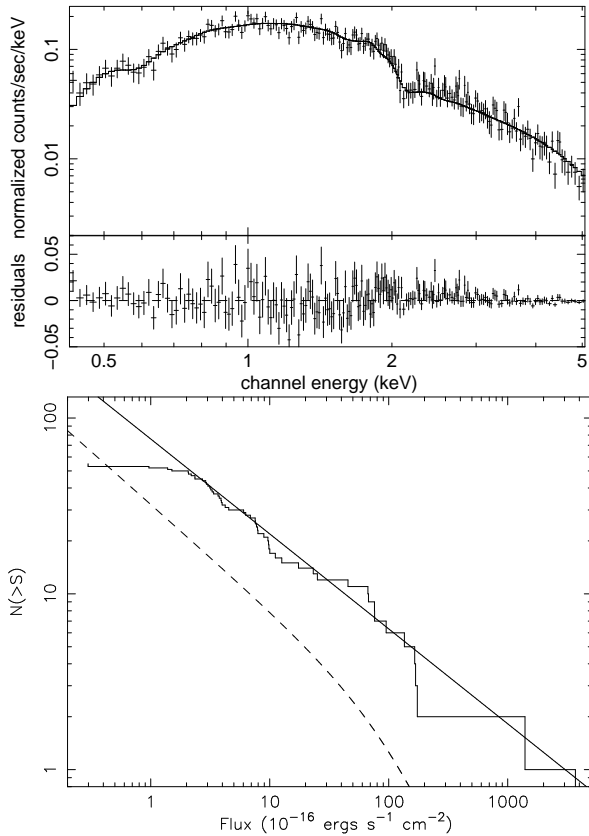


FIG. 2.— Top: The co-added (stacked) spectrum of all 58 discrete sources detected in the *Chandra* X-ray data. The co-added spectrum was constructed using only the first observation. Also shown are the best-fit model (an absorbed bremsstrahlung) and the fit residuals. Bottom: The X-ray luminosity function on the energy range of 0.5–2.0 keV (solid line) for the 58 sources. The best-fit model was used to convert count rates to flux ( $3.1 \times 10^{-4}$  ct  $s^{-1}$  corresponds to  $10^{-15}$  ergs  $cm^{-2}$   $s^{-1}$ ). The single powerlaw model fitted to the luminosity function for sources brighter than  $2 \times 10^{-16}$  ergs  $cm^{-2}$   $s^{-1}$   $\sim 2 \times 10^{35}$  erg  $s^{-1}$  is shown as a solid curve and gives a slope of  $-0.54$ . The dashed curve represents the expected contribution to the luminosity function from cosmic X-ray background sources as given by the Moretti et al. (2003) analytic expression.

If the flux from a source during one observation deviated from its average over the other available observations by  $>3\sigma$ , then it was flagged as long-term variable and designated by the letter “L” in column 5 of Table 2. (Because of differences in spacecraft roll and target aimpoint, not all sources were within the field of view during all four observations.) Short-term variability during individual observations was checked by binning the source light curve (event arrival time) for each observation using 2 ks temporal bins. The shape of the light curve was compared to a constant using the  $\chi^2$  statistic to check for variability. Short-term variability is also given in column 5 of Table 2 by the letter “S”.

The cumulative X-ray luminosity function (XLF) for the 58 sources detected within the  $6' \times 6'$  central region of NGC 2403 is shown in Figure 2. Luminosities for each source were computed from their average flux over up to four observations, depending on availability, on the energy range 0.5–2.0 keV. Using only the 50 sources brighter than a flux limit flux of

$2.0 \times 10^{-16}$  ergs  $cm^{-2}$   $s^{-1}$  in the 0.5–2.0 keV energy range (corresponding to a luminosity at the distance of NGC 2403 of  $2.4 \times 10^{35}$  erg  $s^{-1}$ ), a single power law gives a best-fitting slope of  $-0.54 \pm 0.02$ , roughly consistent with the value of  $-0.59 \pm 0.02$  reported by Schlegel & Pannuti (2003). For reference, a flux of  $10^{-15}$  ergs  $cm^{-2}$   $s^{-1}$  in the 0.5–2.0 keV band corresponds to a flux of  $2.1 \times 10^{-15}$  ergs  $cm^{-2}$   $s^{-1}$  in the 2.0–10.0 keV band assuming our best-fit co-added discrete source spectral shape.

An estimate of the contribution from unrelated background AGN to the detected source population in the field can be made by comparing the observed XLF to the analytical fits to the deep field cosmic X-ray background  $\log N - \log S$  (Moretti et al. 2003). This fit is shown in Figure 2. An estimated  $21 \pm 1$  of the 50 sources, or  $42 \pm 5\%$ , are likely background AGNs.

### 2.3. Supernova Remnants

Most of the individual SNRs (and HII regions discussed in the next subsection) are too faint to be detected as discrete X-ray sources. The possibility exists that many of the X-ray events detected within the spatial regions defined by the individual optical SNRs are unrelated “background” events. Figure 3 shows the XLF for the SNRs. Also shown is a pseudo-random sampling of the background defined using the same locations and sizes of the cataloged SNRs but with their RA coordinates reflected about the center of NGC 2403. (For both populations, only those regions with  $>1$  background-subtracted net counts are shown.) This second XLF indicates that only the (X-ray) brightest 4 or 5 cataloged SNRs are truly sources of X-ray emission. Fitting a single power law model to the XLF of the eight SNRs with  $>4$  source counts in the 0.5–2.0 keV energy range (corresponding to  $1.1 \times 10^{-16}$  ergs  $cm^{-2}$   $s^{-1}$ ) gives a best-fitting slope of  $-0.89 \pm 0.14$ .

There are four optically-identified SNRs detected in X-rays via the source-finding tool. The X-ray-brightest SNR is also the brightest in H $\alpha$  line emission. However, there is no overall correlation between X-ray and H $\alpha$  luminosity in the SNR sample. This is consistent with the analysis of Pannuti et al. (2007). Using the two SNRs whose diameters are listed in Matonick et al. (1997), we also find the mean diameter of X-ray-detected SNRs is smaller (40 pc) than the mean diameter of X-ray non-detections (70 pc) again confirming the Pannuti et al. (2007) result.

A co-added spectrum of the cataloged SNRs was created by merging the first three *Chandra* images (the fourth observation does not adequately cover the central  $6' \times 6'$  region of interest). Twenty-four SNRs (of 27 total) are imaged on S3 in the first three observations. The same averaging method used for the discrete sources (§ 2.2) was used here to build the co-added spectrum. Weighted ARF and RMF files generated from the second observation were used for the spectral fitting. We checked that this did not adversely affect our fitting results by repeating the spectral analysis using ARFs and RMFs generated from the first and third observations.

We used a surrounding annulus to define a local background for the individual SNRs, after masking out the detected X-ray point sources. The total number of X-

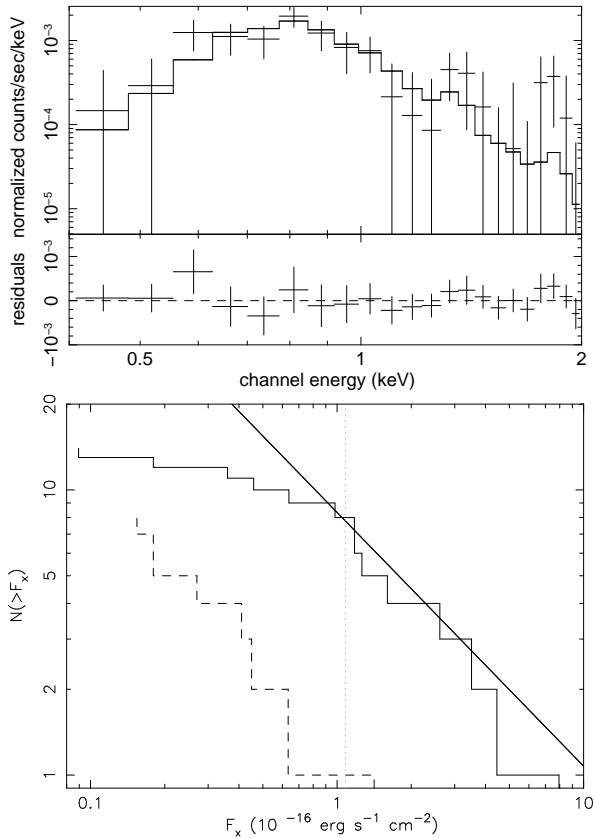


FIG. 3.— Top: The co-added (stacked) spectrum of the 24 optically-identified SNRs imaged on S3. The best-fitting model (an absorbed `apec` model with hydrogen column density,  $N_{\text{H}}$ , allowed to be a free parameter) is shown along with the fit residual. The spectrum has been re-binned to have a width of 73 eV for display purposes. Bottom: The luminosity function of the background-subtracted SNRs (solid line) and of the pseudo-random positions (dashed line, see text). The single powerlaw model fitted to the luminosity function of sources brighter than  $1.1 \times 10^{-16}$  ergs  $\text{cm}^{-2}$   $\text{s}^{-1} \sim 2 \times 10^{35}$  erg  $\text{s}^{-1}$  is shown as a curve and gives a slope of  $-0.89$ .

TABLE 4  
SNRS X-RAY FITTING RESULTS

Fit Parameters	<code>apec</code>	<code>apec</code>	<code>apec</code>
$N_{\text{H}}$ ( $10^{21} \text{cm}^{-2}$ )	0.4	1.4	$2.8^{+3.3}_{-2.3}$
$T_e$ (MK)	$4.8^{+2.6}_{-1.0}$	$4.2^{+1.6}_{-0.7}$	$3.5^{+2.1}_{-1.4}$
Normalization <sup>a</sup>	$0.1^{+0.5}_{-0.1}$	$0.3^{+0.1}_{-0.1}$	$0.5^{+2.3}_{-0.5}$
$L_X/10^{37}$ erg $\text{s}^{-1}$	$0.3^{+0.1}_{-0.1}$	$0.3^{+0.1}_{-0.1}$	$0.3^{+0.5}_{-0.2}$
$L_X^{int}/10^{37}$ erg $\text{s}^{-1}$	0.3	0.6	0.8
C-stat/bins	107.4/108	105.9/108	105.3/108
Derived Parameters <sup>b</sup>			
$V [f]$ ( $10^{63} \text{cm}^3$ )	0.13	0.13	0.13
$n_e [f^{-1/2}]$ ( $\text{cm}^{-3}$ )	0.04	0.05	0.07
$P/k [f^{-1/2}]$ ( $10^5 \text{K cm}^{-3}$ )	3.5	4.1	5.1
$M_x [f^{+1/2}]$ ( $10^5 M_{\odot}$ )	0.05	0.07	0.11
$E_{th} [f^{+1/2}]$ ( $10^{53}$ erg)	0.09	0.1	0.1
$t_c [f^{+1/2}]$ (Myr)	48	30	16

<sup>a</sup>  $K = (10^{-9}/4\pi D^2) \int n_e n_p dV$

<sup>b</sup> volume filling factor scaling in  $[ ]$  in Column 1.

ray events in the co-added spectrum between 0.4 and 2.0 keV is 153. This reduces to  $94.8 \pm 13.1$  after background subtraction. The XSPEC model `apec`, representing thermal emission from an optically-thin collisionally-ionized plasma, combined with a model `phabs` for an intervening absorption column were applied to the spectrum. The parameters of the `apec` model are the plasma temperature, elemental abundances, and emission integral. Elemental abundances were fixed to the solar values as given in Anders & Grevesse (1989). Three model fits were attempted as detailed in Table 4. These differed in the values assigned to the absorbing columns. In two of these models, the absorbing column was held fixed at either the Galactic value along the line of sight,  $N_{\text{H}}^g = 4 \times 10^{20} \text{cm}^{-2}$ , implying no local absorption within NGC 2403, or  $N_{\text{H}} = 14 \times 10^{20} \text{cm}^{-2}$  which is equivalent to the mean value of the optical extinction derived for active star-forming regions (§ 3). The third model allows the absorbing column to be a free parameter in the fit. In this and in models of the HII regions and of the residual X-ray emission to be discussed below, allowing the absorbing column, plasma temperature, and normalization (emission integral) to vary in the fitting process often leads to large uncertainties in some of these parameter values. The reason for this is simply that the plasma temperature is quite low, of order a few  $10^6$  K (a few 0.1 keV), so that most of the emission is at low energies where the sensitivity to absorption is most acute. This introduces a degeneracy in which an equally acceptable fit is possible by increasing the column density,  $N_{\text{H}}$ , while simultaneously increasing the model normalization, usually with a moderate decrease in the fitted temperature.

The X-ray luminosities of the individual SNRs were computed by adopting the spectral model that best fits the stacked spectrum (Table 4, column 4). This model was applied to the distribution of events of each individual SNR using the best-fit values of  $T_e$  and  $N_{\text{H}}$ , and allowing only the model normalization to vary in the final fitting. This is equivalent to scaling by the number of counts in the individual spectra. The X-ray count rates, corresponding luminosities, and  $\text{H}\alpha$  luminosities are listed in Table 5.

A number of other physical parameters can be derived from the fitted values of the plasma temperature and emission integral provided some estimate of the volume occupied by the hot gas can be made. The total volume of the 24 SNRs is  $1.3 \times 10^{62} \text{cm}^3$  assuming a spherical geometry for each remnant and adopting the radii reported in Matonick et al. (1997; the same radii used here to define the X-ray spectral source regions). The actual volume occupied by the hot gas is some fraction,  $f$ , of this total volume. Assuming the ion and electron number densities are equal, which is roughly true for a hydrogen-dominated hot plasma, then the emission integral  $\int n_e n_H dV \sim n_e^2 fV$  so that the electron density  $n_e \propto (K/fV)^{1/2}$  where  $K$  is the spectral model normalization parameter which is itself proportional to the emission integral.

From  $n_e$  and the flux-weighted mean temperature  $T_e$ , we can estimate the hot gas pressure  $P/k = 2n_e T_e$ , mass  $M_X = n_e \mu m_p V$  where  $m_p$  is the proton mass and  $\mu = 1.4$  is the mass per proton, thermal energy  $E_{th} = 3n_e V k T_e$  and the cooling time  $t_c = E_{th}/L_{\text{bol}}$  of the X-ray emitting

TABLE 5  
SNRs

RA (J2000)	Dec (J2000)	Count Rate <sup>a</sup> 10 <sup>-5</sup> cts s <sup>-1</sup>	$L_X$ <sup>b</sup> 10 <sup>35</sup> erg s <sup>-1</sup>	$L_{H\alpha}$ 10 <sup>37</sup> erg s <sup>-1</sup>
07 36 42.8	+65 34 52.7	-0.8 ± 1.0	-0.3 ± 0.4	0.3
07 36 45.7	+65 36 35.7	1.1 ± 1.5	0.4 ± 0.6	1.7
07 36 45.7	+65 36 40.7	25.8 ± 4.8	10.0 ± 1.8	17.1
07 36 49.0	+65 34 31.0	3.3 ± 3.8	1.3 ± 1.5	2.4
07 36 52.0	+65 33 41.0	-0.5 ± 0.9	-0.2 ± 0.3	0.5
07 36 52.7	+65 35 50.5	-0.8 ± 1.0	-0.3 ± 0.4	4.8
07 36 53.3	+65 36 00.3	3.8 ± 2.0	1.5 ± 0.8	1.0
07 36 53.5	+65 33 42.0	2.4 ± 2.1	0.9 ± 0.8	5.5
07 36 53.6	+65 35 11.6	-0.5 ± 0.9	-0.2 ± 0.3	2.9
07 36 56.2	+65 34 06.0	5.1 ± 2.7	2.0 ± 1.1	1.8
07 36 57.0	+65 36 04.8	-0.5 ± 0.9	-0.2 ± 0.3	0.3
07 37 01.6	+65 34 13.0	7.8 ± 3.4	3.0 ± 1.3	2.9
07 37 02.0	+65 34 37.0	0.0 ± 0.9	0.0 ± 0.4	5.5
07 37 02.0	+65 33 42.0	0.3 ± 0.9	0.1 ± 0.3	0.4
07 37 02.2	+65 37 20.7	1.0 ± 1.2	0.4 ± 0.5	2.3
07 37 02.2	+65 36 02.0	3.7 ± 1.8	1.5 ± 0.7	2.9
07 37 03.0	+65 33 45.0	0.0 ± 0.9	0.0 ± 0.4	0.3
07 37 03.0	+65 34 38.0	10.1 ± 2.9	3.9 ± 1.1	1.0
07 37 06.0	+65 36 03.2	-2.4 ± 1.8	-0.9 ± 0.7	2.0
07 37 06.1	+65 36 10.3	-0.8 ± 1.7	-0.3 ± 0.7	2.2
07 37 07.1	+65 37 10.6	-1.3 ± 1.0	-0.5 ± 0.4	1.2
07 37 10.6	+65 33 10.0	2.8 ± 1.9	1.1 ± 0.7	0.3
07 37 12.5	+65 33 46.0	0.5 ± 0.8	0.2 ± 0.3	2.0
07 37 16.1	+65 33 29.0	13.2 ± 3.3	5.1 ± 1.3	0.8

Units of right ascension are hours, minutes, and seconds, and units of declination are degrees, arcminutes, and arcseconds.

<sup>a</sup> Count rates for ACIS-S3, taking the 0.5 – 2.0 keV energy band.

<sup>b</sup> Luminosity in the 0.5 – 2.0 keV energy band.  $L_X$  is computed using the one temperature model with variable  $N_H$  model as listed in Table 4 (see text)

plasma as listed in Table 4. Here,  $L_{bol}$  is estimated by integrating the spectral model from 0.02 keV to 20 keV within XSPEC. For plasma temperature typical of SNRs (and of other thermal sources analyzed in this paper),  $L_{bol}$  is  $\sim 5$  times  $L_X$ , where  $L_X$  is the observed X-ray luminosity quoted on the standard 0.5–2.0 keV range. These derived quantities are all functions of the volume filling factor,  $f$  as indicated in the table.

The total X-ray luminosity from the 24 SNRs is only  $3 \times 10^{36}$  erg s<sup>-1</sup>. Inspection of Figure 3 shows that most of this emission comes from the few brightest sources with the most luminous being  $\sim 1 \times 10^{36}$  erg s<sup>-1</sup>. The thermal energy content of the SNRs,  $\sim 10^{52} f^{1/2}$  erg, corresponds to up to  $\sim 40\%$  (in the limit  $f = 1$ ) of the initial kinetic energy released by the supernova explosions, assuming  $10^{51}$  erg per event. The total mass of hot gas is substantial. It corresponds to an average mass per SNR of  $M_X \sim 300 \pm 100 f^{1/2} M_\odot$  (uncertainties given by the range of values deduced from the three X-ray spectral models). This can be compared to the amount of material swept up by the SNRs,  $\sim 5000 n_H M_\odot$  per SNR, assuming a uniform density  $n_H$  cm<sup>-3</sup>, over the SNR volume.

#### 2.4. HII Regions

We performed an analysis of the 48 HII regions, imaged on S3 in the first three observations, analogous to that of the SNRs. Figure 4 shows the XLF for the HII regions and the pseudo-random sampling defined using RA coordinates reflected about the center of NGC 2403. Again, only the most X-ray-luminous HII regions are significant detections. Similar to the SNRs, we also fitted a single power law model to the XLF of the 7

brightest HII regions, ( $>4$  counts and corresponding to  $1.1 \times 10^{-16}$  ergs cm<sup>-2</sup> s<sup>-1</sup>). The best-fitting slope is  $-0.47 \pm 0.13$ , somewhat shallower than for the SNRs.

The co-added X-ray spectrum is shown in Figure 4. Similar to the SNR spectrum, we also applied thermal models to the HII region spectrum. There are sufficient source counts (858 cts,  $422 \pm 32$  after the background subtraction) in the HII region spectrum to allow 2-temperature model fits in addition to the 1-temperature models that were applied to the SNR spectrum. The fitting results and derived values are listed in Table 6. We assumed pressure equilibrium between the two temperature components and identical filling factors to derive the values of  $n_e$ ,  $E_{th}$ , and  $M_x$ .

Note that the best-fitting 1-temperature model with variable column density results in a very high model normalization which leads to unreasonable values of the derived parameters. However, this does not seem to be the issue with the 2-temperature model. This model (column 6 in Table 6) results in  $N_H \sim N_H^g$  (though with large uncertainty) and hence with values of the remaining parameters similar to those of the fixed  $N_H$  model.

The X-ray luminosities of the individual HII regions were computed in the same manner as for the SNRs; using the best-fitting two temperature spectral model with variable  $N_H$  in this case. The X-ray count rates, corresponding luminosities, and H $\alpha$  luminosities are listed in Table 7.

There are twice as many HII regions in our sample as there are SNRs in our SNR sample. The X-ray temperatures of the HII regions are about 40% lower compared to the SNRs. The total X-ray luminosity is  $\sim 1.5 \times 10^{37}$  erg s<sup>-1</sup> for the HII regions which is only a

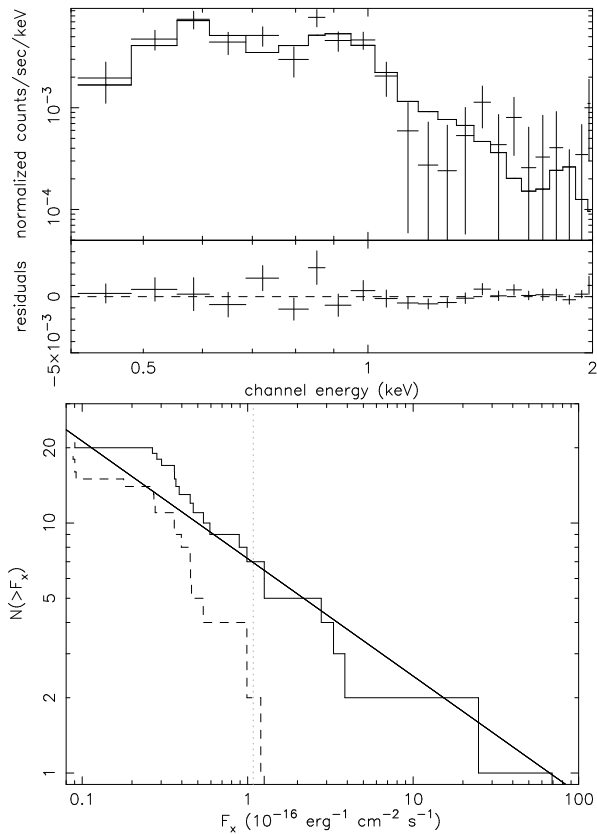


FIG. 4.— Top: The stacked spectrum of the identified HII regions. The best-fitting model (an absorbed two-temperature `apec` model with hydrogen column density,  $N_{\text{H}}$ , as a free parameter) is shown along with the fit residuals. The spectrum has been re-binned to have a width of 73 eV for display purposes. Bottom: The luminosity function of the background-subtracted HII regions (solid line) and of the pseudo-random positions (dashed line, see text). The single powerlaw model fitted to the luminosity function of sources brighter than  $1.1 \times 10^{-16} \text{ erg cm}^{-2} \text{ s}^{-1} \sim 2 \times 10^{35} \text{ erg s}^{-1}$  is shown as a curve and gives a slope of  $-0.47$ .

factor of 3 higher, on average, for individual HII regions compared to the SNRs. Similarly, the average hot gas mass is  $\sim 1000 M_{\odot}$ , per HII region, based on the best-fitting 2-temperature spectral model. This is about a factor of 3 larger than the hot gas mass in individual SNRs.

### 2.5. Residual Emission

The left panel of Figure 5 displays a smoothed image of the soft X-ray emission from the underlying unresolved component. This residual emission is defined as the net emission left after masking out all detected point sources (including SN 2004dj and TH2), HII regions and SNRs. For spectral fitting, an X-ray map of this component was created using only the first *Chandra* observation. This is a compromise in that a deeper image could be made using an image merged from two or more individual observations but the area of the region of overlap sampled by these multiple observations is too small to define both a sizable source region and a surrounding background region that are both wholly contained within the overlap region (see Figure 1). The first *Chandra* observation placed the center of NGC 2403 near the S3 aimpoint and

thus is the most useful for our purposes. The source region is defined as a disk of radius  $2\frac{1}{2}$  (2.3 kpc) centered on NGC 2403. The background is composed of three non-contiguous regions of low surface brightness as shown in Figure 1. To construct the smoothed image depicted in Figure 5, all excluded regions were filled with a local background level using the Poisson method of the CIAO tool `dmfilth`<sup>6</sup>, then divided by an exposure map evaluated at an energy of 0.5 keV. This exposure-corrected image was then smoothed using the CIAO tool `aconvolve` using a Gaussian function with a width of 10 pixels ( $\sim 5''$ ).

There are several nearly point-like regions that remain in the residual emission image. These may be faint point sources that were hidden in the PSF wings of brighter nearby sources or extended non-spherical features in HII regions not covered by our (circular) masks. We examined the five brightest of these regions and find they contribute only 4% of the counts in the residual emission spectrum. Therefore, these regions were left in as part of the residual emission.

In general, the residual emission fills a broad region of the central part of NGC 2403 extending from northwest of the nucleus (located at the center of the image) to southeast of the nucleus. This region is not a particularly strong source of emission at UV, mid-IR, nor  $\text{H}\alpha$  wavelengths. For example, a grayscale UV image is shown in the right panel of Figure 5 with the X-ray contours overlaid. This image suggests that much of the residual X-ray emission is centrally located relative to the UV-bright zones that contain stars  $\lesssim 100$  Myrs old.

Several models were fitted to the spectrum of this residual X-ray emission. Area-weighted ARFs and RMFs were created for this purpose using the CIAO script `specextract`. The spectral fitting results are listed in Table 8.

The three thermal models with the absorption column density frozen during the fitting all give low values for the model normalization, electron density, pressure, hot gas mass, and thermal energy. The best-fitting of these models is the 2-temperature model with temperatures of 2.3 and 8.6 MK with most of the flux in the cooler component (Table 8, column 5), shown in Figure 6. Fixing the absorption column density to the Galactic value implies that the residual emission lies above the disk of NGC 2403 where there is little or no overlying cold gas. This is a reasonable assumption if the X-ray-emitting gas was ejected from the galaxy through galactic-scale winds or smaller fountains or chimneys. Fixing the absorption column density to the equivalent mean value of the optical extinction toward the active star-forming regions in NGC 2403,  $N_{\text{H}} = 1.4 \times 10^{21} \text{ cm}^{-2}$ , corresponds to a modest layer of overlying cold gas.

The models with the absorption column density free to vary during the fit result in statistically improved fits with absorbing columns higher than found for any of the other types of X-ray sources considered in the previous subsections. Such high columns imply that the hot gas is located behind a layer of neutral gas such as would be the case if the hot gas were confined to the disk. However, the observed HI column densities through the central disk of NGC 2403

<sup>6</sup> See [http://cxc.harvard.edu/ciao/threads/diffuse\\_emission/](http://cxc.harvard.edu/ciao/threads/diffuse_emission/)



TABLE 6  
HII REGIONS X-RAY FITTING RESULTS

Fit Parameters	apec	apec	apec	apec+apec	apec+apec
$N_H$ ( $10^{21}$ cm $^{-2}$ )	0.4	1.4	$7.8^{+1.5}_{-0.8}$	0.4	$0.4^{+2.3}_{-0.0}$
$T_{e1}$ (MK)	$3.5^{+0.4}_{-0.3}$	$3.0^{+0.6}_{-0.2}$	$1.1^{+0.4}_{-0.2}$	$1.8^{+0.6}_{-0.5}$	$1.8^{+0.6}_{-0.5}$
Normalization $K_1$ <sup>a</sup>	$0.7^{+0.1}_{-0.1}$	$1.5^{+0.3}_{-0.4}$	$2153^{+33590}_{-1991}$	$0.8^{+0.1}_{-0.3}$	$0.8^{+1.7}_{-0.2}$
$T_{e2}$ (MK)				$8.8^{+2.0}_{-1.2}$	$8.8^{+1.0}_{-1.4}$
Normalization $K_2$				$0.3^{+0.1}_{-0.1}$	$0.3^{+0.2}_{-0.1}$
$L_X/10^{37}$ erg s $^{-1}$	$1.2^{+0.2}_{-0.2}$	$1.2^{+0.2}_{-0.3}$	$1.3^{+0.5}_{-1.0}$	$1.4^{+0.2}_{-0.4}$	$1.4^{+0.1}_{-0.2}$
$L_X^{int}/10^{37}$ erg s $^{-1}$	1.5	2.7	365	1.7	1.7
C-stat/bin	154.0/108	151.9/108	129.4/108	120.3/108	120.3/108
Derived Parameters <sup>b</sup>					
$V$ [ $f$ ] ( $10^{63}$ cm $^3$ )	2.2	2.2	2.2	2.2	2.2
$n_e$ [ $f^{-1/2}$ ] (cm $^{-3}$ )	0.02	0.03	1.1	0.07,0.01	0.07,0.01
$P/k$ [ $f^{-1/2}$ ] ( $10^5$ K cm $^{-3}$ )	1.4	1.9	40	2.5	2.5
$M_x$ [ $f^{+1/2}$ ] ( $10^5 M_\odot$ )	0.5	0.8	28	0.5	0.5
$E_{th}$ [ $f^{+1/2}$ ] ( $10^{53}$ erg)	0.6	0.9	18	1.1	1.1
$t_c$ [ $f^{+1/2}$ ] (Myr)	55	32	0.1	32	32

<sup>a</sup>  $K = (10^{-9}/4\pi D^2) \int n_e n_p dV$

<sup>b</sup> volume filling factor scaling in [ ] in Column 1.

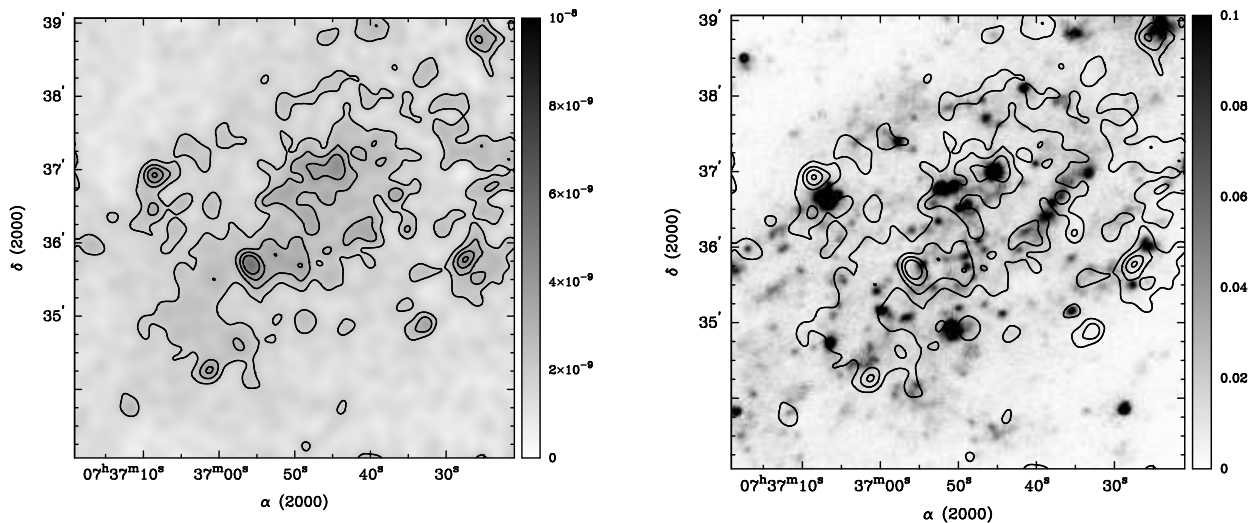


FIG. 5.— The residual X-ray emission from NGC 2403. Left: The soft X-ray image (0.4–2.0 keV) of the central  $6' \times 6'$  region. All four observations have been co-added and exposure-corrected and all discrete sources, optically-identified SNRs and HII regions have been removed. The image has been aggressively smoothed with the CIAO tool `aconvolve`. The contours indicate 10, 20, 30, and  $40\sigma$  above the background level. The gray scale indicates intensity levels in units of photon cm $^{-2}$  s $^{-1}$  pixel $^{-1}$ . One pixel corresponds to  $0''.492$ . Right: The X-ray residual emission contours overlaid on the GALEX FUV image. The gray scale of the image indicates intensity levels in units of ct s $^{-1}$  pixel $^{-2}$ . One pixel corresponds to  $1''.5$ .

range from only  $\sim 10^{21}$  cm $^{-2}$  (Thornley & Wilson 1995) to  $\sim 3 \times 10^{21}$  cm $^{-2}$  (Schaap et al. 2000; Fraternali et al. 2002b) which is considerably less than implied by these X-ray model fits, suggesting the models are unphysical. Furthermore, inspection of the images of this hot gas component and comparison to images at other wavelengths suggest that the hot gas is not emitted from regions with high levels of overlying cold gas.

Therefore, the models with the absorption column fixed are the most realistic models. They imply  $(4 - 7) \times 10^6 M_\odot$  of hot gas is present in the central regions of NGC 2403, assuming a 2.3 kpc radius spherical emission volume. This hot gas is rather tenuous,  $n_e \sim 0.003$  to  $0.004$  cm $^{-3}$ , with, formally, a long cooling time of 200 – 340 Myr. We note that the actual X-ray emitting re-

gion is slightly smaller than the 2.3 kpc radius spectrum extracting region, so that the assumed volume may be larger than the volume containing the hot gas. If we assume instead that the hot gas is confined to a disk with thickness 200 pc and 2.3 kpc radius, then the inferred density increases by about a factor of 4 in compensation for the smaller volume for a given emission integral. This reduces the cooling time to 50 – 90 Myrs. The true emission volume is probably somewhere between our sphere and disk estimates. Table 8 contains derived properties of the residual gas for both these geometries.

An estimate of the contribution to this residual X-ray emission from unresolved sources fainter than, but otherwise similar to, the discrete source population (§2.2) can be made by extrapolating the fitted point-source lu-

TABLE 7  
HII REGIONS

R.A. J2000	Decl J2000	Count Rate <sup>a</sup> 10 <sup>-4</sup> cts s	$L_X$ <sup>b</sup> 10 <sup>35</sup> erg s <sup>-1</sup>	$L_{H\alpha}$ 10 <sup>37</sup> erg s <sup>-1</sup>
07 36 35.7	+65 35 09.0	3.8 ± 2.9	1.6 ± 1.3	16.4
07 36 38.0	+65 36 09.5	1.6 ± 1.5	0.7 ± 0.6	2.3
07 36 38.4	+65 36 23.7	3.0 ± 2.3	1.3 ± 1.0	5.7
07 36 39.6	+65 37 11.5	0.3 ± 0.9	0.1 ± 0.4	2.2
07 36 41.7	+65 38 06.7	-0.2 ± 1.4	-0.1 ± 0.6	31.6
07 36 44.6	+65 35 07.7	3.8 ± 2.4	1.6 ± 1.0	6.1
07 36 45.6	+65 36 59.9	9.8 ± 7.3	4.2 ± 3.1	147.7
07 36 45.7	+65 36 37.4	0.8 ± 1.6	0.4 ± 0.7	0.9
07 36 45.9	+65 36 40.6	-0.3 ± 0.8	-0.1 ± 0.3	0.1
07 36 45.9	+65 37 14.6	-0.8 ± 1.9	-0.3 ± 0.8	3.5
07 36 46.7	+65 36 36.9	1.4 ± 2.9	0.6 ± 1.2	5.4
07 36 46.9	+65 37 05.3	-1.7 ± 2.5	-0.7 ± 1.1	3.6
07 36 47.1	+65 35 42.5	-1.9 ± 1.8	-0.8 ± 0.8	6.6
07 36 47.2	+65 36 44.8	-0.8 ± 1.7	-0.3 ± 0.7	2.3
07 36 47.4	+65 37 00.1	-0.4 ± 1.9	-0.2 ± 0.8	1.2
07 36 47.6	+65 35 53.5	1.1 ± 1.8	0.5 ± 0.8	2.5
07 36 47.9	+65 34 34.8	0.0 ± 0.9	0.0 ± 0.4	2.2
07 36 48.1	+65 33 26.3	0.0 ± 1.6	0.0 ± 0.7	7.0
07 36 49.2	+65 36 33.5	-1.6 ± 2.2	-0.7 ± 0.9	8.5
07 36 49.3	+65 36 52.9	-3.8 ± 1.4	-1.6 ± 0.6	14.3
07 36 50.0	+65 35 11.2	-0.5 ± 1.4	-0.2 ± 0.6	4.8
07 36 50.4	+65 35 28.6	-1.6 ± 1.7	-0.7 ± 0.7	2.8
07 36 50.9	+65 34 57.7	-2.4 ± 1.2	-1.0 ± 0.5	6.1
07 36 52.3	+65 36 47.3	74.1 ± 10.3	31.9 ± 4.4	140.7
07 36 52.9	+65 36 20.7	-2.1 ± 1.2	-0.9 ± 0.5	3.5
07 36 53.2	+65 36 34.7	-0.8 ± 1.0	-0.3 ± 0.4	0.8
07 36 53.2	+65 34 14.4	-1.1 ± 1.0	-0.5 ± 0.4	3.8
07 36 53.4	+65 35 28.4	-0.3 ± 1.3	-0.1 ± 0.6	1.2
07 36 54.5	+65 35 47.8	-1.6 ± 1.7	-0.7 ± 0.7	4.1
07 36 55.6	+65 34 11.0	-0.3 ± 1.9	-0.1 ± 0.8	1.9
07 36 57.8	+65 37 24.5	2.7 ± 4.4	1.1 ± 1.9	67.1
07 36 59.4	+65 35 09.1	0.8 ± 1.9	0.3 ± 0.8	1.3
07 36 60.0	+65 35 06.8	-2.4 ± 1.4	-1.1 ± 0.6	2.1
07 37 00.3	+65 35 11.0	1.1 ± 2.6	0.5 ± 1.1	5.8
07 37 00.8	+65 35 25.2	11.5 ± 4.3	5.0 ± 1.9	15.7
07 37 03.7	+65 36 19.9	-0.8 ± 0.9	-0.3 ± 0.4	2.9
07 37 05.8	+65 35 52.3	1.1 ± 1.5	0.5 ± 0.7	3.9
07 37 07.0	+65 36 41.1	206.1 ± 16.6	88.8 ± 7.2	448.2
07 37 10.6	+65 35 42.2	-0.2 ± 1.9	-0.1 ± 0.8	6.3
07 37 11.1	+65 34 36.7	-0.8 ± 1.0	-0.3 ± 0.4	3.0
07 37 11.6	+65 33 56.2	1.8 ± 1.5	0.8 ± 0.6	1.5
07 37 11.7	+65 33 59.5	0.9 ± 1.6	0.4 ± 0.7	2.4
07 37 11.8	+65 33 49.0	-1.6 ± 2.0	-0.7 ± 0.8	5.3
07 37 14.0	+65 36 10.0	-1.9 ± 1.1	-0.8 ± 0.5	1.7
07 37 16.4	+65 34 03.5	1.3 ± 2.4	0.6 ± 1.0	5.3
07 37 18.6	+65 35 41.7	1.2 ± 2.5	0.5 ± 1.1	8.2
07 37 18.7	+65 33 50.6	8.3 ± 3.7	3.6 ± 1.6	36.2

NOTE. — Units of right ascension are hours, minutes, and seconds, and units of declination are degrees, arcminutes, and arcseconds.

<sup>a</sup> Count rates for ASIC-S3, taking the 0.5 – 2.0 keV energy band.

<sup>b</sup> Luminosity in the 0.5 – 2.0 keV energy band.  $L_X$  is computed using the two temperature model with variable  $N_H$  model listed in Table 6.

minosity function slope (Figure 2) to lower luminosities. For this, we scale the XLF to include only those sources within the 2'5 residual emission region. Using the same absorbed bremsstrahlung model as before (§ 2.2) results in an estimated unresolved point source contribution of  $2 \times 10^{37}$  erg s<sup>-1</sup> in the 0.5 to 2.0 keV energy range or about a 10–15% contribution to the diffuse emission. As an alternative estimate, we added a bremsstrahlung model component to the hot gas spectral model to estimate the contribution from unresolved sources. Adding a bremsstrahlung component does not improve statistical significance of the fit but can contribute up to ~20% of the flux in the 0.5–2.0 keV band. The contributions from SNRs and HII regions to the residual X-ray emis-

sion can also be estimated from their XLFs (Figures 3, and 4). These estimates are  $9 \times 10^{36}$  erg s<sup>-1</sup> for the SNRs and  $1 \times 10^{36}$  for the HII regions. The estimated contribution from SNRs is relatively high because the XLF slope is steep for this source population. In any event, faint SNRs and HII regions can contribute only a small fraction to the total X-ray luminosity of the residual emission which is  $1.6 \times 10^{38}$  erg s<sup>-1</sup> or higher.

#### 2.6. Discussion of Preliminary Analysis of X-ray Observations

The bulk X-ray properties of the SNRs, HII regions, and diffuse (residual) emission are summarized in Tables 4, 6, and 8, respectively. They show that the hot

TABLE 8  
RESIDUAL EMISSION X-RAY FITTING RESULTS

Fit Parameters	apec	apec	apec	apec+apec	apec+apec
$N_H$ ( $10^{21}$ cm $^{-2}$ )	0.4	1.4	$5.6^{+1.0}_{-1.7}$	0.4	$5.2^{+3.6}_{-1.0}$
$T_{e1}$ (MK)	$3.1^{+0.3}_{-0.2}$	$2.8^{+0.2}_{-0.1}$	$1.7^{+0.2}_{-0.3}$	$2.3^{+0.4}_{-0.3}$	$1.7^{+0.1}_{-1.7}$
Normalization K <sub>1</sub> <sup>a</sup>	$9.0^{+0.9}_{-1.0}$	$17.2^{+1.9}_{-1.8}$	$820^{+1716}_{-459}$	$7.7^{+1.3}_{-1.2}$	$642^{+2639}_{-432}$
$T_{e2}$ (MK)				$8.6^{+1.3}_{-1.2}$	$45.5^{+697}_{-27.0}$
Normalization K <sub>2</sub>				$2.5^{+0.6}_{-0.7}$	$9.2^{+13.8}_{-5.4}$
$L_X/10^{38}$ erg s $^{-1}$	$1.3^{+0.2}_{-0.2}$	$1.3^{+0.2}_{-0.2}$	$1.5^{+0.2}_{-1.1}$	$1.5^{+0.3}_{-0.3}$	$1.7^{+0.4}_{-0.9}$
$L_X^{int}/10^{38}$ erg s $^{-1}$	1.6	3.1	70	1.9	56.9
C-stat/bin	140.7/108	133.9/108	106.6/108	105.9/108	97.1/108
Derived Parameters <sup>b</sup>					
$V_{sphere}^c [f]$ ( $10^{63}$ cm $^3$ )	1535	1535	1535	1535	1535
$n_e [f^{-1/2}]$ (cm $^{-3}$ )	0.003	0.004	0.026	0.006,0.002	0.08,0.003
$P/k [f^{-1/2}]$ ( $10^5$ K cm $^{-3}$ )	0.2	0.2	0.8	0.3	2.5
$M_x [f^{+1/2}]$ ( $10^5 M_\odot$ )	47	66	460	43	167
$E_{th} [f^{+1/2}]$ ( $10^{53}$ erg)	51	67	270	90	830
$t_c [f^{+1/2}]$ (Myr)	311	203	7.3	342	30
$V_{disk}^d [f]$ ( $10^{63}$ cm $^3$ )	97	97	97	97	97
$n_e [f^{-1/2}]$ (cm $^{-3}$ )	0.01	0.01	0.10	0.023,0.006	0.31,0.01
$P/k [f^{-1/2}]$ ( $10^5$ K cm $^{-3}$ )	0.7	0.8	3.3	1.1	10
$M_x [f^{+1/2}]$ ( $10^5 M_\odot$ )	11	17	114	11	42
$E_{th} [f^{+1/2}]$ ( $10^{53}$ erg)	12	17	66	23	211
$t_c [f^{+1/2}]$ (Myr)	78	51	1.8	86	7.5

For two temperature models, the average  $n_e$  is estimated as  $M_x/(\mu m_p V)$  and used in text.

<sup>a</sup>  $K = (10^{-9}/4\pi D^2) \int n_e n_p dV$

<sup>b</sup> Volume filling factor scaling in [ ] in Column 1.

<sup>c</sup> A 2.3 kpc radius spherical emission volume.

<sup>d</sup> A disk with the thickness 200pc and 2.3 kpc radius.

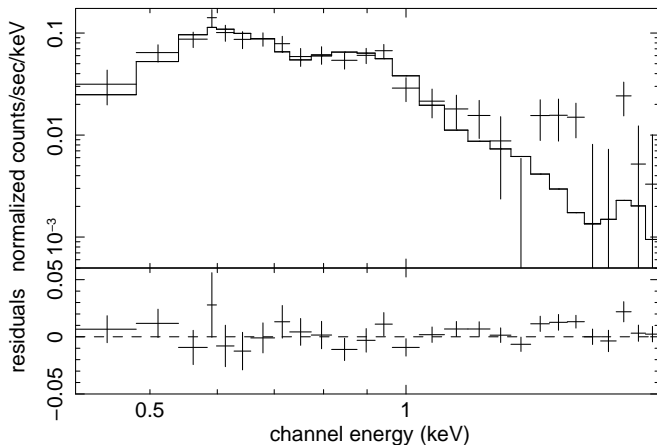


FIG. 6.— The X-ray spectrum of the residual emission from the central  $6' \times 6'$  region of NGC 2403. Data from only the first observation are included. The best-fitting model, a two-temperature apec model with hydrogen column density fixed to the galactic value, and the fit residuals are shown. The spectrum has been re-binned to have a width of 73 eV for display purposes.

gas densities in SNRs and HII regions are comparable but that the SNR temperature is somewhat higher resulting in higher pressures,  $P \propto nT_X$ , by about a factor of 2. This is not surprising since the SNR, which must have ages of order  $10^4$  yr or less (Matonick et al. 1997), are expected to be further from pressure equilibrium with their surroundings than the fully-developed HII regions which have ages of  $10^6$  to  $>10^7$  yr.

Another difference between the SNRs and HII regions is the amount of hot gas estimated from the X-ray data. There is, on average, about  $300 \pm 100 M_\odot$  of hot gas per

SNR compared to about  $1000 M_\odot$  per HII region. Of course, HII regions are composed of many stars and SNs whereas the SNRs identified by Matonick et al. (1997) are morphologically consistent with single events. Evidently, SNe occurring within the relatively tenuous and hot interior of HII regions are much less efficient at producing hot gas than are isolated SNe. The ratio of the hot gas mass to the swept up mass for SNRs is therefore  $\sim 0.06$ – $0.10$  and for the HII regions it is only  $\sim 0.03$  for an assumed ambient density of  $1 \text{ H cm}^{-3}$ . This indicates, again, that shock heating and thermal evaporation from the swept-up shells of young isolated SNRs is more efficient than in HII regions.

The diffuse (residual) emission has a density and pressure lower by about a factor of 10 (assuming the spherical volume) compared to SNRs and HII regions but a temperature that is comparable to both these sources. If we assume a disk geometry, then the density is closer to the density in SNRs and HII regions. There is another parameter to consider. The volume filling factor,  $f$ , may be lower for this residual emission compared to the SNRs and HII regions because, by definition, this residual shares the galaxy disk with the much colder neutral and molecular gas and dust. Assuming  $f \sim 1$  for the HII regions and pressure equilibrium suggests a filling factor  $f \sim (0.2 - 0.3)$  for the residual emission with correspondingly higher density and shorter cooling time. Alternatively, we may assume pressure equilibrium between the hot residual gas component and the colder gas and dust. This cold gas resides primarily in clouds of typical temperatures of  $T \sim 100$  K and densities of  $60$ – $100 \text{ cm}^{-3}$ . This corresponds to a typical pressure  $P/k \sim 10^4 \text{ cm}^{-3} \text{ K}$  which would imply, at the observed temperature of  $(2-3) \times 10^6 \text{ K}$ , a hot gas density

of  $\sim 0.003\text{--}0.005\text{ cm}^{-3}$  consistent with the derived value (Table 8) if  $f \sim 1$ . We note (Fraternali et al. 2002b) that the mean HI density in the central regions of NGC 2403 is about  $0.4\text{ cm}^{-3}$ . Thus its filling factor must be only around 5% for a cloud density of  $80\text{ cm}^{-3}$ . A similar argument can be made for the  $\text{H}_2$  content (Sheth et al. 2005). Thus the filling factors for the cold gas may be quite small so that the bulk of the volume in the central regions of NGC 2403 may be filled with hot gas at high filling factor ( $f \sim 1$ ). This, in turn, would imply a considerable overpressure in the HII regions which is not wholly unreasonable.

In any case, the mass of hot gas in this residual component,  $M_X \lesssim 7 \times 10^6 M_\odot$ , is a small fraction of the mass contained in HI ( $5 \times 10^8 M_\odot$ ) and comparable to the molecular ( $8 \times 10^6 M_\odot$ ) gas mass.

We cannot tell with certainty where this X-ray emitting residual gas is located. There is not a strong spatial correlation between this gas and star-formation indicators including  $\text{H}\alpha$  and UV emission. Combining this fact with an estimated cooling time of up to 340 Myr (depending on the geometry assumed and the filling factor) allows for several possibilities. The residual gas may have been created *in situ* during star-formation activity that ended up to 100 Myr ago (in regions currently lacking strong UV emission) or it may have been produced more recently but has escaped from its place of origin either into the halo or into low-density regions of the disk.

At this point, we only have crude estimates of the ages of the various star-forming regions that are present in the central regions of NGC 2403. The ages of HII regions are  $\lesssim 10$  Myr, equivalent to the lifetimes of the least-massive LyC-producing stars. The ages of UV-emitting regions can be as old as 100 Myr. What is needed is a better estimate of the age of individual star-forming regions. From this, we can better estimate how X-ray properties evolve through time and so better constrain the origin of the residual X-ray emission – whether it traces recent star-formation activity or is a relic of past activity. This is the subject of the next section.

### 3. INDIVIDUAL STAR-FORMING REGIONS AND THEIR ANALYSIS

We now turn to the analysis of individual young star-forming regions that have well-defined ages and masses. We choose young regions because they are more likely sources of X-ray emission from hot gas than are older clusters; and have more likely retained their identity as a coherent (though not necessarily bound) and coeval system under the prevailing tidal forces. Theoretically, X-ray emission from stellar winds and hot gas associated with supernovae (SNe) occurs only within the first  $\sim 40$  Myr in the lifetime of a star cluster corresponding to the longest-lived stars that become core collapse SNe, roughly the  $8\text{--}10 M_\odot$  stars. Star clusters in this age range emit strongly in UV light and (during the first  $\sim 10$  Myr) in  $\text{H}\alpha$  line emission. However, these star-formation indicators are sensitive to extinction by overlying dust. Dust heated by UV and optical radiation emits this energy in the mid-IR and longer wavelength bands. Therefore, we define our regions as those bright in both UV radiation from massive young stars and in mid-IR radiation from reprocessing by dust. In this way, we can better estimate the extinction along the line of sight us-

ing the mid-IR flux and thus correct the UV emission to obtain a better estimate of the age and mass of the star clusters.

Star-formation tends to propagate spatially by compressing surrounding colder regions of the interstellar medium through the action of massive star winds and supernovae. Thus, small isolated regions are more likely to have a single characteristic age than are large extended regions. Therefore, we apply our source-finding algorithm to identify isolated star-forming regions quantitatively rather than to rely on a pre-determined object size (such as a fixed aperture or spatial grid, for instance, which is known to sample a range of stellar ages; cf., Calzetti et al. 2005). The drawback to our selection method is that the flux from individual regions may be weak at wavelengths other than the UV and mid-IR we use to select them.

#### 3.1. Complementary Observations

We use *GALEX* UV and *Spitzer* mid-IR measurements to identify young star-forming regions. We also use  $\text{H}\alpha$ , a traditional star-formation tracer, in our analysis to confirm a young age for the regions.

*GALEX* observed NGC 2403 on December 5, 2003 (Tilenum 5087) as part of the Nearby Galaxy Survey (Gil de Paz et al. 2007). Corrected intensity maps at FUV ( $1529\text{ \AA}$  central wavelength) and NUV ( $2321\text{ \AA}$ ) were obtained from the *GALEX* archive<sup>7</sup>. The images have a pixel scale of  $1.5''$  and a spatial resolution of about  $5''$ . We applied the standard flux calibrations of  $1.40 \times 10^{-15}\text{ ergs cm}^{-2}\text{ s}^{-1}\text{ cts}^{-1}\text{ \AA}^{-1}$  to the FUV and  $2.06 \times 10^{-16}\text{ ergs cm}^{-2}\text{ s}^{-1}\text{ cts}^{-1}\text{ \AA}^{-1}$  to the NUV images.

NGC 2403 was observed with *Spitzer* IRAC and MIPS as a part of the Spitzer Infrared Nearby Galaxies Survey (SINGS) legacy program (Kennicutt et al. 2003). MIPS images at  $24\text{ }\mu\text{m}$  were taken on 2004 October 13 and 16 (key 5549568 and 5549824, respectively). The IRAC  $3.6\text{ }\mu\text{m}$ , and  $4.5\text{ }\mu\text{m}$  images were taken on 2004 October 8 (key 5505792) and 12 (key 5505536). Final mosaiced images provided by the SINGS program were used here. Details of their data reduction and calibration are reported in the SINGS data delivery paper<sup>8</sup>. The  $24\text{ }\mu\text{m}$  image has an  $\sim 5''$  resolution which is comparable to *GALEX*. The final mosaiced image has a pixel scale of  $1.5''$ . Both the IRAC images have a spatial resolution of  $\sim 2''$  and a pixel scale of  $0.75''$ .

As part of the SINGS project, NGC 2403 was observed with the Kitt Peak National Observatory 2.1m telescope in  $\text{H}\alpha$  bands on 2001 November 8. We obtained a continuum-subtracted  $\text{H}\alpha$  image, made by subtracting an *R*-band image from a narrow-filter image at  $\text{H}\alpha$  (D. Calzetti, private communication). The pixel scale of the  $\text{H}\alpha$  image is  $0.3''$  and the resolution is about  $1''$ . The  $\text{H}\alpha$  flux is estimated from this image by assuming the  $[\text{NII}]/\text{H}\alpha$  ratio and final  $\text{H}\alpha$  correction factor as given in Prescott et al. (2007).

As with the X-ray data, SN 2004dj was used to define a common registration among the data sets. Unsaturated, foreground stars were used to register pre-

<sup>7</sup> <http://galex.stsci.edu/GR2/>

<sup>8</sup> [http://data.spitzer.caltech.edu/popular/sings/20070410.enhanced\\_v1/Docu](http://data.spitzer.caltech.edu/popular/sings/20070410.enhanced_v1/Docu)

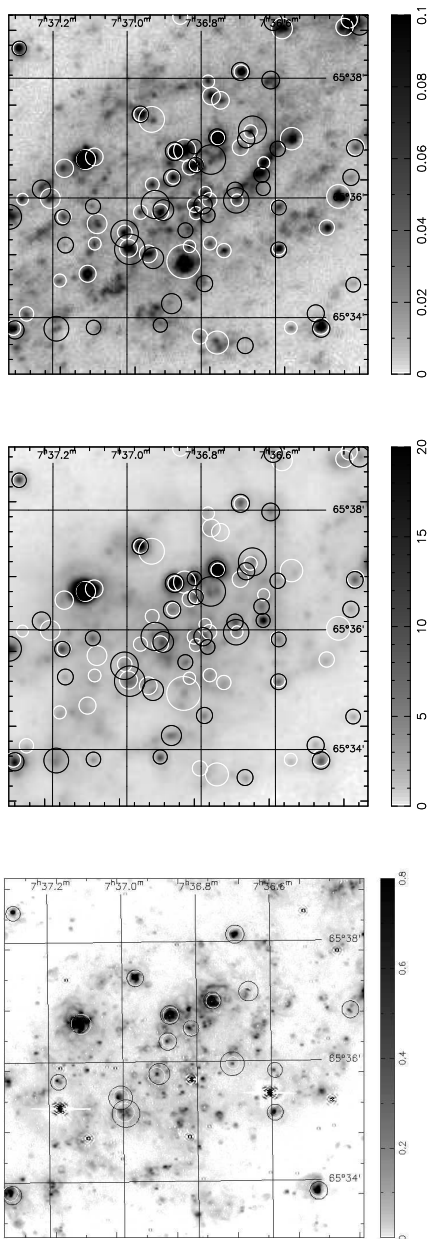


FIG. 7.— Identification of star-forming regions in NGC 2403. Top: The central  $6' \times 6'$  region of NGC 2403 at FUV (*GALEX*  $\lambda 1529 \text{ \AA}$ ). The positions of the 58 sources detected in the FUV band are encircled in white. The positions of the 47 sources detected at  $24 \mu\text{m}$  are encircled in black. The sizes of the circles indicate photometric apertures defined as the  $3\sigma$  width of a circular Gaussian model fitted to the respective surface brightness distribution. The gray scale is the same as the right panel of Figure 5. Middle: The same region at  $24 \mu\text{m}$  (*Spitzer*). Symbols same as for the FUV image. The gray scale indicate intensity levels in units  $\text{MJy str}^{-1}$  for  $24 \mu\text{m}$  image. One pixel corresponds to  $1''/5/\text{pixel}$ . Bottom: The 19 sources common to both FUV and  $24 \mu\text{m}$  images overlaid on the continuum-subtracted  $\text{H}\alpha$  image. Sixteen of the 19 sources were also selected as HII regions as described in § 2.4. The gray scale indicate intensity level in the units  $\text{ct s}^{-1} \text{ pixels}^{-2}$ , which corresponds to  $2.1 \times 10^{-6} \text{ Jy pixels}^{-2}$ . The image has a pixel scale of  $0''.304$ .

supernova ground-based, and *GALEX* images.

### 3.2. Star-forming Region Definitions

The same source finding tool applied to the X-ray images was used to identify candidate star-forming regions in the FUV and  $24 \mu\text{m}$  images. This tool is optimized for detecting point sources but can be applied to moderately-extended sources by increasing the characteristic size of the model PSF parameter. We used a circular Gaussian PSF in the application because most of the star-forming regions appeared centrally-peaked at the moderate resolution of the  $24 \mu\text{m}$  and FUV images. We examined their radial profiles *post facto* using the higher resolution  $\text{H}\alpha$  images to confirm that they are basically extended and either centrally-peaked or centrally-cratered so that the Gaussian model is adequate for estimating both the emission centroids and the spatial extent.

We detected 58 bright sources in the central  $6' \times 6'$  FUV image (Figure 7, top panel) defined as those with a  $S/N$  above 10 and with a minimum of 15 source counts per unit uncertainty in the background. Similarly, 47 bright sources are detected in the  $24 \mu\text{m}$  image (Figure 7, middle panel) with a  $S/N$  above 50 and with 100 or more electrons per unit uncertainty in the background. There are 19 sources common to both the FUV and  $24 \mu\text{m}$  images. These 19 regions are shown in Figure 7 (bottom panel) overlaid on the  $\text{H}\alpha$  image. (Sixteen of these regions were selected as HII regions based on their  $\text{H}\alpha$  brightness in §2.4.)

This constitutes our star-forming region sample. The sample is only representative of the star-forming regions in NGC 2403; a larger sample could be made by including regions of lower  $S/N$ . Note (Figure 7) that there are sources brighter than these 19 in one or the other of the two selection wavebands, but not in both. Examining all available images, none of the sample regions have properties of foreground stars or of background AGN.

The observed luminosities and angular sizes of the 19 regions are listed in Table 9. We performed aperture photometry on the individual sources with corresponding aperture sizes for each region and waveband. Although these 19 sources are extended, in order to define sizes of aperture, we apply the circular Gaussian model. The radii in each region and each band are determined as  $3\sigma$  circular Gaussian widths, which contains 99% of flux of the sources. For most regions, a surrounding annulus that extends to twice the source's aperture radius was used for background. In more crowded regions, a non-contiguous nearby region was used instead. Luminosities are computed using definitions similar to those used by the SINGS team (e.g., Calzetti et al. 2005); specifically,  $L_{\text{band}} = \lambda L_{\lambda, \text{band}}$  for broad bands and  $L_{\text{band}} = \delta \lambda L_{\lambda, \text{band}}$  for narrow bands. Luminosities were corrected for the Galactic extinction along the line of sight,  $E_{B-V} = 0.040 \text{ mag}$  (Schlegel et al. 1998), with the Cardelli et al. (1989) dust model. The aperture correction values listed on the *Spitzer* web page were applied to the  $24 \mu\text{m}$  data. Thumbnail images in the FUV and  $24 \mu\text{m}$  bands are shown in Figure 8. The circles shown in these images define the adopted radii in each band. Note that they are rarely concentric. Also shown in Figure 8 are the  $\text{H}\alpha$  radial profiles for each region.

The sizes of the regions in the FUV band are systematically smaller than in the  $\text{H}\alpha$  and  $24 \mu\text{m}$  bands. The

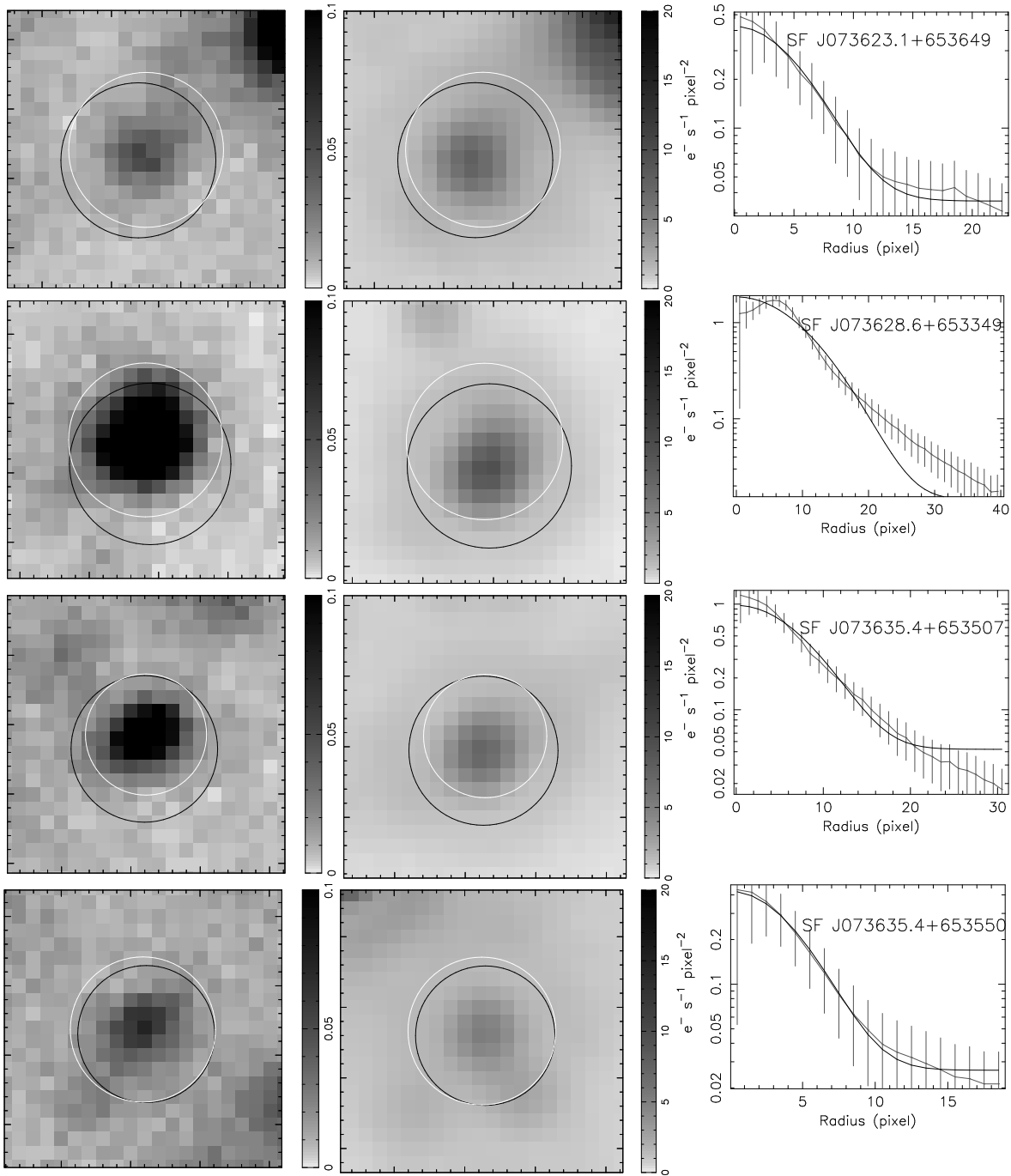


FIG. 8.—  $30'' \times 30''$  close-up views of the 19 star-forming regions. FUV images are on the left and  $24\mu\text{m}$  images are in the middle. Circle locations, sizes, colors, and gray scales are the same as in Figure 7. On the right are higher-resolution  $\text{H}\alpha$  radial profiles shown with best-fitting Gaussian model curves. Each radial profile extends to 5 Gaussian widths. One pixel corresponds to  $0.''304$ . (First four are shown here. The rest of the 15 regions are shown at the end of the paper.)

natural interpretation is that the FUV originates from young star clusters whereas the source of  $\text{H}\alpha$  and  $24\mu\text{m}$  is re-radiation from surrounding warm ionized gas and cold dust regions, respectively, that lie at the outskirts of wind-blown bubbles created by the stars. This is also the reason why the regions are not concentric in the different wavebands. The  $\text{H}\alpha$  radial profiles, Figure 8, which often show a crater-like morphology is also indicative of this shell-like structure.

### 3.3. Age, Mass, & Extinction Determinations

The five wavelength bands FUV, NUV (both from *GALEX*),  $3.6\mu\text{m}$ ,  $4.5\mu\text{m}$ , and  $24\mu\text{m}$  (all from *Spitzer*) were used to define the spectral energy distributions (SEDs) of light from the individual regions. These were compared to theoretical spectra of instantaneous starbursts based on the models of Leitherer et al. (1999) as improved by Vázquez & Leitherer (2005) by convolv-

TABLE 9  
LUMINOSITIES AND SIZES OF 19 STAR-FORMING REGIONS

SRC	$L_{FUV}$ $10^{39} \text{erg s}^{-1}$	$R_{FUV}$ arcsec	$L_{NUV}$ $10^{39} \text{erg s}^{-1}$	$L_{3.6\mu m}$ $10^{38} \text{erg s}^{-1}$	$L_{4.5\mu m}$ $10^{38} \text{erg s}^{-1}$	$L_{24\mu m}$ $10^{39} \text{erg s}^{-1}$	$R_{24\mu m}$ arcsec	$L_{H\alpha}$ $10^{38} \text{erg s}^{-1}$	$R_{H\alpha}$ arcsec	$L_X^{obs}$ $10^{35} \text{erg s}^{-1}$
SF J073623.1+653649	4.8 ± 0.3	8.4	2.9 ± 0.1	4.1 ± 0.2	2.7 ± 0.1	4.1 ± 0.1	8.4	0.8	8.5	9.7 ± 4.4
SF J073628.6+653349	30.2 ± 1.5	8.3	20.4 ± 0.6	5.6 ± 0.2	4.8 ± 0.1	4.9 ± 0.1	8.7	7.4	8.8	8.9 ± 4.4
SF J073635.4+653507	10.0 ± 0.5	6.5	5.6 ± 0.2	5.7 ± 0.2	3.3 ± 0.1	2.3 ± 0.1	7.9	3.0	8.0	8.5 ± 4.2
SF J073635.4+653550	4.9 ± 0.3	7.8	2.8 ± 0.1	3.2 ± 0.2	2.0 ± 0.1	1.9 ± 0.0	7.4	0.7	7.5	1.2 ± 2.9
SF J073639.5+653709	5.4 ± 0.3	6.7	3.7 ± 0.1	2.9 ± 0.2	1.8 ± 0.1	3.1 ± 0.1	9.7	1.2	9.8	7.7 ± 4.6
SF J073641.6+653806	18.6 ± 1.0	7.0	10.6 ± 0.3	6.3 ± 0.2	4.7 ± 0.2	5.0 ± 0.1	9.1	4.5	9.2	7.1 ± 4.3
SF J073642.3+653557	4.3 ± 0.3	6.0	3.3 ± 0.1	3.7 ± 0.3	2.3 ± 0.2	4.7 ± 0.1	11.8	1.0	11.9	21.6 ± 6.5
SF J073645.4+653700	148.9 ± 7.5	6.8	106.5 ± 3.2	30.8 ± 0.6	22.7 ± 0.4	43.9 ± 0.9	8.5	16.7	8.6	24.8 ± 6.3
SF J073648.9+653633	23.1 ± 1.2	7.3	19.8 ± 0.6	8.3 ± 0.4	7.2 ± 0.2	5.2 ± 0.1	7.7	1.5	7.8	9.0 ± 4.2
SF J073652.3+653646	69.6 ± 3.5	7.5	53.3 ± 1.6	19.7 ± 0.5	13.9 ± 0.3	36.4 ± 0.7	9.3	15.2	9.4	63.0 ± 9.2
SF J073652.7+653620	7.5 ± 0.4	6.7	5.9 ± 0.2	2.6 ± 0.4	0.8 ± 0.1	3.7 ± 0.1	8.7	1.1	8.8	7.9 ± 4.3
SF J073654.1+653547	13.1 ± 0.7	8.2	12.0 ± 0.4	3.7 ± 0.4	2.5 ± 0.2	10.9 ± 0.2	10.4	2.0	10.5	24.1 ± 6.5
SF J073657.8+653723	16.3 ± 0.8	7.3	11.2 ± 0.3	21.3 ± 0.5	14.5 ± 0.3	18.2 ± 0.4	8.2	7.8	8.4	11.8 ± 5.0
SF J073659.6+653508	22.6 ± 1.2	9.0	16.3 ± 0.5	14.0 ± 0.5	9.8 ± 0.3	9.5 ± 0.2	13.6	4.0	13.8	26.7 ± 7.8
SF J073700.4+653524	9.0 ± 0.5	7.3	7.3 ± 0.2	2.1 ± 0.2	2.0 ± 0.1	4.7 ± 0.1	11.7	3.0	11.9	21.9 ± 6.5
SF J073706.6+653638	150.9 ± 7.6	9.9	107.5 ± 3.2	81.9 ± 1.4	61.2 ± 1.0	168.1 ± 3.4	9.0	35.7	9.1	98.0 ± 11.2
SF J073710.4+653540	3.9 ± 0.3	6.9	5.2 ± 0.2	3.5 ± 0.2	2.5 ± 0.1	4.3 ± 0.1	7.8	1.2	7.8	0.9 ± 2.9
SF J073717.4+653829	18.7 ± 1.0	6.8	12.3 ± 0.4	2.1 ± 0.1	2.0 ± 0.1	4.2 ± 0.1	7.2	3.2	7.3	0.5 ± 3.0
SF J073718.0+653347	16.9 ± 0.9	7.4	11.1 ± 0.3	5.4 ± 0.2	9.4 ± 0.2	13.1 ± 0.3	9.1	6.7	9.2	5.2 ± 4.4

NOTE. — FUV, NUV, and H $\alpha$  luminosities are Galactic extinction corrected.

TABLE 10  
DERIVED VALUES OF 19 STAR-FORMING REGIONS

SRC	Mass $10^5 M_\odot$	Age Myr	$A_V$	$N_H$ $10^{21} \text{cm}^{-2}$	$L_w$ $10^{38} \text{erg s}^{-1}$	$L_{FUV}^{int}$ $10^{39} \text{erg s}^{-1}$	$L_{H\alpha}^{int}$ $10^{38} \text{erg s}^{-1}$	$L_X^{int}$ $10^{35} \text{erg s}^{-1}$
SF J073623.1+653649	0.4	9	0.67	1.7	5.2	9.8 ± 0.3	1.3	23.5 ± 10.7
SF J073628.6+653349	0.7	8	0.22	0.8	9.9	33.8 ± 0.3	8.6	13.7 ± 6.8
SF J073635.4+653507	0.8	16	0.32	1.0	7.5	12.8 ± 0.2	3.7	14.6 ± 7.2
SF J073635.4+653550	0.3	11	0.44	1.2	3.5	7.4 ± 0.2	0.9	2.2 ± 5.6
SF J073639.5+653709	0.3	9	0.5	1.4	3.9	8.8 ± 0.2	1.7	16.1 ± 9.7
SF J073641.6+653806	0.7	9	0.35	1.1	9.0	24.8 ± 0.3	5.7	12.7 ± 7.8
SF J073642.3+653557	0.4	9	0.65	1.6	5.2	08.5 ± 0.3	1.6	50.2 ± 15.1
SF J073645.4+653700	2.4	1	0.3	1.0	26.7	185.6 ± 0.8	20.6	49.2 ± 12.5
SF J073648.9+653633	0.9	9	0.25	0.9	11.6	26.9 ± 0.3	1.8	14.6 ± 6.9
SF J073652.3+653646	1.5	1	0.44	1.2	16.7	104.7 ± 0.6	20.8	142.5 ± 20.8
SF J073652.7+653620	0.3	8	0.44	1.2	4.2	11.3 ± 0.3	1.4	15.0 ± 8.2
SF J073654.1+653547	0.3	2	0.54	1.4	4.7	22.5 ± 0.4	2.9	61.8 ± 16.7
SF J073657.8+653723	17.5	60	0.67	1.7	0.0	33.2 ± 0.5	12.7	27.5 ± 11.5
SF J073659.6+653508	10	50	0.4	1.2	0.0	32.2 ± 0.4	5.4	49.5 ± 14.4
SF J073700.4+653524	0.3	7	0.46	1.3	4.7	13.8 ± 0.3	4.2	43.8 ± 13.0
SF J073706.6+653638	6.4	1	0.71	1.7	71.2	325.2 ± 1.3	59.3	302.5 ± 34.5
SF J073710.4+653540	0.4	9	0.57	1.5	5.2	6.9 ± 0.3	1.8	2.1 ± 6.5
SF J073717.4+653829	0.2	2	0.27	0.9	3.1	22.4 ± 0.3	3.9	0.8 ± 5.7
SF J073718.0+653347	0.4	1	0.56	1.5	4.5	29.7 ± 0.4	9.9	14.1 ± 11.9

NOTE. — Listed  $N_H$  values include a Galactic component of  $N_H = 0.4 \times 10^{21} \text{cm}^{-2}$ .

ing these spectra with the spectral response functions of the appropriate filters. For computing the theoretical spectra, we assumed the Kroupa (2001) initial mass function (IMF), namely a power-law IMF on the range 0.1–100  $M_\odot$  with a break at 0.5  $M_\odot$  and slopes of 1.3 below and 2.3 above the break. A solar metallicity was assumed; consistent with estimates from the literature (e.g., Martin & Belley 1996; Garnett et al. 1997). We accounted approximately for the wavelength-dependent attenuation by dust by using the starburst dust model of Calzetti (2001). We modeled the re-emission of this radiation in the mid-IR by assuming energy conservation and a blackbody emission profile at a temperature of 75 K. This temperature was estimated by fitting a blackbody curve to the *Spitzer* MIPS 24, 70, and 160  $\mu\text{m}$

measurements from the brightest of our star-forming regions. (This region is fully resolved and isolated even in the 160  $\mu\text{m}$  image so that a distinct local background could be identified.) Varying the blackbody temperature by  $\sim 30\%$  has little impact on our results. However, much higher or lower temperatures result in unrealistic estimates of the age and mass of several of the star-forming regions.

By using five-band SEDs we are thus able to sample the UV region which is most sensitive to age in young star clusters yet is most affected by dust attenuation, the near-IR at 3.6 and 4.5  $\mu\text{m}$  that is least affected by dust and hence is sensitive primarily to cluster mass, and the mid-IR 24  $\mu\text{m}$  which lies within the dust emission band that extends from several microns out to much longer

wavelengths. The  $24\ \mu\text{m}$  waveband is longward of the PAH emission features which greatly complicate the dust emission spectrum (e.g., Pérez-González et al. 2006) but shortward of the lower spatial resolution long wavelength *Spitzer* bands.

We used a least-squares fit of the model SEDs to the observed luminosities using equal weights for each spectral band. Operationally, the model extinction and cluster mass parameters were allowed to vary, at a fixed cluster age, until a minimum  $\chi^2$  was found. We then repeated this process for discrete cluster ages ranging from 1 to 200 Myr (in steps of 1 Myr for ages  $\leq 20$  Myr and steps of 10 Myr otherwise) to obtain the overall best-fitting age, mass, and extinction combination. That is, we do not interpolate the model spectra to intermediate ages.

The results are summarized in Table 10. In addition to the best-fitting mass, age, and extinction values based on the SEDs fitting, Table 10 also includes the corresponding hydrogen column density,  $N_{\text{H}} = (A_V/R_V)5.8 \times 10^{21}\ \text{cm}^{-2}$ , assuming an optical parameter  $R_V = 3.1$ , and the corresponding observed  $\text{H}\alpha$ , and FUV luminosities after correcting for extinction.

Among the most massive young clusters in our sample are the giant HII regions NGC2403-I and NGC2403-II studied by Drissen et al. (1999). Drissen et al. estimate the ages of these clusters as between 2 and 6 Myr based on their detection of Wolf-Rayet stars in these regions. A crude estimate of the initial cluster mass can be made from the number of WR stars detected. This estimate is very sensitive to the upper mass cutoff assumed of the initial mass function and, of course, to the true age of the cluster. Interestingly, the age and mass values obtained from the studies of Drissen et al. are consistent with our findings and independently validates our SED fitting method. Garnett et al. (1999) estimated line-of-sight extinction to several of our sample star-forming regions from Balmer line ratios. Our estimates are in agreement with these results within  $A_V$  of 0.3 mag. For example, we derive  $A_V = 0.7$  mag for the brightest HII region, compared to  $A_V = 0.6$  mag from Balmer line ratios (Garnett et al. 1999) and to  $A_V = 0.9$  mag from extinction toward blue giants in the region (Drissen et al. 1999).

The best-fitting ages of the regions fall into three distinct ranges,  $<3$  Myr, from 7 to 16 Myr, and  $>50$  Myr which we designate young, intermediate, and old, respectively. We believe the two regions designated as old are likely younger than their best-fitting ages. Inspection of the distribution of the  $\chi^2$  fit statistic shows, for these two old regions, that there is a second local minimum at 13 Myr which is probably a more realistic age estimate. Note that they have moderately high FUV luminosities, by selection, which, for their fitted age, forces their best-fitting mass to be very high relative to the other groups. There is not a similar trend in the fitted extinction values.

There are distinct differences among the members of the remaining two age groups. Members of the young group are typically much more luminous, per unit mass, at UV,  $\text{H}\alpha$ , and  $24\ \mu\text{m}$  compared to the intermediate age group members. Based on the star cluster model, the UV luminosity is expected to rise slightly during the

first 4 Myr then drop rapidly as the most massive stars become supernovae. Similarly, the  $\text{H}\alpha$  luminosity, which comes from recombination of circumstellar gas photoionized by massive stars, also drops quickly as these massive stars disappear. The observed trends are consistent with this scenario.

Dust emission, accounting for most of the  $24\ \mu\text{m}$  luminosity, also represents re-radiation of starlight. It is most sensitive to UV but also responds to longer wavelength light. One would expect, therefore, that the  $24\ \mu\text{m}$  luminosity per unit mass would decrease more slowly than would the UV and  $\text{H}\alpha$  luminosities. However, as the cluster evolves and its wind-driven bubble expands, surrounding dust clouds will evaporate and the solid angle subtended by remaining dust clouds will decrease. This could account for the rapid drop with age observed in the  $24\ \mu\text{m}$  luminosity.

These trends do not apply to the near-IR 3.6 and  $4.5\ \mu\text{m}$  luminosities. Light at these wavelengths comes directly from stars of practically all masses (ages) and is not strongly affected by dust. Thus, the near-IR luminosity per unit mass is nearly independent of the age of the underlying star cluster; as observed.

One puzzling result is that the young star forming regions in our sample are much more massive than the intermediate-age regions. The average mass of the young regions is  $1.9 \times 10^5\ M_{\odot}$  and only  $0.5 \times 10^5\ M_{\odot}$  for the intermediate-age regions. Notably, there is one region that is 3 times as massive as any other. Excluding this region, the average mass of the young group is still twice that of the intermediate group. This may be an indication of a selection bias. If more massive star clusters more efficiently destroy or disperse surrounding dust clouds, then our selection criterion that requires regions be bright in both UV and  $24\ \mu\text{m}$  would tend to select against more massive clusters. Naturally, the destruction of dust takes time so this bias may only work against massive intermediate-age star-forming regions. Comparison of the two panels of Figure 7 shows that there are several regions bright in UV that lack a strong IR counterpart. In particular, there is a very UV-bright region just below the center of the field at  $L_{\text{FUV}}^{\text{int}} \sim 7 \times 10^{40}\ \text{erg s}^{-1}$ . This cluster was not selected because it lacks strong dust emission. It is likely of intermediate age as it also is weak in  $\text{H}\alpha$  emission. Assuming an age of 10-15 Myr suggests a mass in the range of about  $2 \times 10^5$  to  $4 \times 10^5$  based on the values of  $L_{\text{FUV}}^{\text{int}}$  for the clusters listed in Table 10. This makes this cluster more massive than all but the two most massive young clusters.

Crude estimates of the star-formation rate in the central regions of NGC 2403 can be made from the values listed in Table 10. The total mass in stars in the young age group clusters is  $1.1 \times 10^6\ M_{\odot}$ . These stars were formed in the recent 2 Myr interval for a mean star-formation rate of  $0.5\ M_{\odot}\ \text{yr}^{-1}$ . Adding the contribution from the intermediate-age group gives  $1.7 \times 10^6\ M_{\odot}$  of stars formed over a 16 Myr period or a  $0.1\ M_{\odot}\ \text{yr}^{-1}$  average rate. These rates can be compared to rates deduced from  $\text{H}\alpha$  luminosities. For the young age group clusters this rate is only  $0.1\ M_{\odot}\ \text{yr}^{-1}$  and is only slightly higher when the intermediate-age clusters are included (see Table 10). The two methods give quite different estimates. It is unlikely that the escape fraction of ionizing radiation is large enough to compensate for the discrepancy.



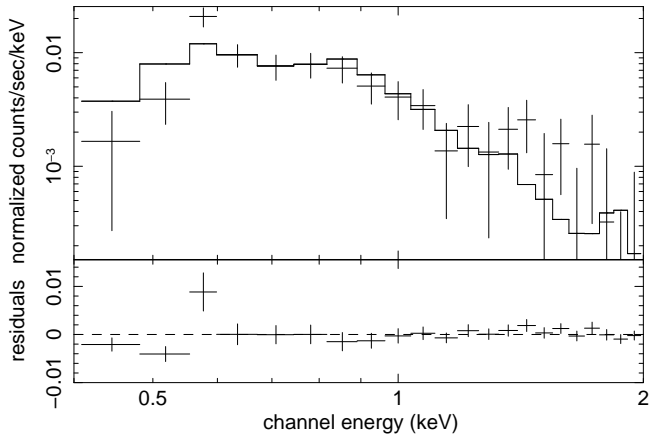


FIG. 9.— Co-added spectrum of the 6 young star-forming regions. The best-fitting model, an absorbed two-temperature *apec* model with the hydrogen column density allowed as a free parameter, and the fit residual are also shown. The spectrum has been re-binned to have a width of 73 eV for display purposes.

Finally, the values can be compared to the galaxy-wide star-formation rate of  $1.3 M_{\odot} \text{ yr}^{-1}$  based on the  $\text{H}\alpha$  luminosity and assuming a nominal  $A(\text{H}\alpha) = 1$  mag reported by Kennicutt et al. (2003). This suggests that 10% or up to 38% of the current galaxy-wide star formation is occurring within these 19 star clusters. This is not an unreasonable estimate since the brightest few clusters in the sample clearly dominate the relevant emission from NGC 2403.

#### 3.4. Comparison to X-ray Properties

In most cases, the X-ray emission from these individual star-forming regions is too faint to be detected as a discrete source using our standard source-detection algorithm. Therefore, we define the X-ray source radius for each region to be the largest of the values determined from fitting the surface brightness distribution in the UV, mid-IR, and  $\text{H}\alpha$  bands. Furthermore, we combine (stack) the spectra of the young and of the intermediate age regions to accumulate sufficient counts for fitting of the spectra of these two age groups. For this purpose, we used the first observation only, in which all regions are imaged on the S3 CCD. We used the same background as was used for analysis of the residual emission (§2.5) and apply the same one- and two-temperature thermal emission models described in §2 to the stacked spectra. Due to low counts, only the one-temperature models are applied to the intermediate age region stacked spectrum. We calculated mass-weighted  $A_V$  from the SED fitting (§3.3) for both groups and calculated a corresponding  $N_H$ , namely  $1.4 \times 10^{21} \text{ cm}^{-2}$  for the young and  $1.1 \times 10^{21} \text{ cm}^{-2}$  for the intermediate regions. The fitting results are shown in Tables 11 and 12 for the young and intermediate age star-forming regions, respectively. The spectra with best-fitting models are shown in Figure 9 for the young regions and Figure 10 for the intermediate

regions. Not surprisingly, the star-forming regions have X-ray temperatures and densities similar to the HII regions selected by their  $\text{H}\alpha$  brightness (Table 6 and §2.4). These values are somewhat lower than for isolated SNRs (Ta-

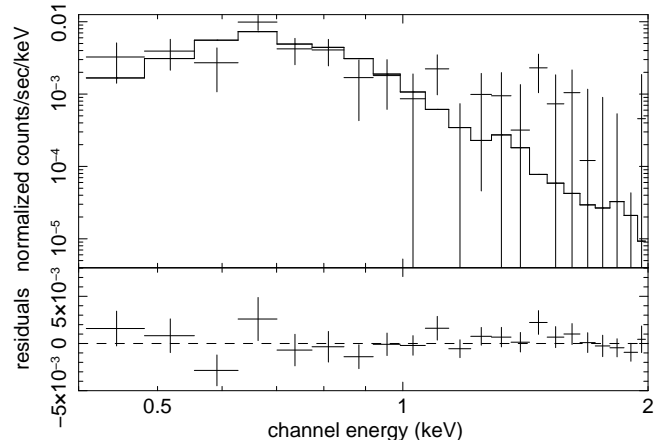


FIG. 10.— Co-added spectrum of the 11 intermediate-age star-forming regions. The best-fitting model, an absorbed one-temperature *apec* model with the hydrogen column density allowed as a free parameter, and the fit residual are also shown. The spectrum has been re-binned to have a width of 73 eV for display purposes.

ble 4) and the densities are higher than deduced for the residual emission (Table 8). The largest differences are found for the intermediate-age group: the derived electron density and pressure are a factor of two lower than that of the HII regions. For models allowing the intervening column density to vary, the resulting  $N_H$  are comparable to the Galactic value or about a factor of ten lower than for any of the other source populations considered including the young star-forming region group.

These results indicate that the star clusters begin to show their age even after just 10–20 Myrs. Their hot gas densities and hence pressures begin to fall although their temperatures remain a moderate 2–3 MK. These values of density and pressure are still higher than the residual emission analyzed in §2.5. Note that most of the LyC-producing stars will have become SNe by the age of 10–20 Myrs so that the traditional current star-formation tracer,  $\text{H}\alpha$ , will no longer be strong.

We can estimate the X-ray luminosities of the individual star-forming regions by scaling by the ratio of counts in the stacked spectra (for each age group) to the number of counts detected in individual regions. The results are listed in Table 10. These luminosities have been corrected for extinction local to each region using the values of  $N_H$  tabulated in column 7 of Table 10 (derived from their best-fitting  $A_V$ ) and for Galactic extinction. The luminosities were computed using the two temperature model with variable  $N_H$  for the young region group, and the one temperature model with variable  $N_H$  for the intermediate age regions.

Figures 11 through 13 compare these intrinsic X-ray luminosities to the (extinction-corrected) FUV,  $24 \mu\text{m}$ , and  $\text{H}\alpha$  luminosities, respectively. In all cases, there is only a weak correlation between X-ray luminosity and these star-formation indicators. This is due to the large scatter in the X-ray luminosities.

A simple calculation shows that in one or two regions a relatively high X-ray luminosity may be the result of a faint undetected X-ray point source in the region. From the XLF, §2.2, we expect about 20 X-ray point sources

TABLE 11  
YOUNG REGIONS X-RAY FITTING PARAMETERS

Fit Parameters	apec	apec	apec	apec+apec	apec+apec
$N_{\text{H}}$ ( $10^{21} \text{ cm}^{-2}$ )	0.4	1.4	$4.7^{+1.7}_{-1.1}$	0.4	$2.9^{+2.0}_{-2.0}$
$T_{e1}$ (MK)	$3.4^{+0.3}_{-0.3}$	$3.0^{+0.5}_{-0.2}$	$2.1^{+0.3}_{-0.5}$	$2.8^{+0.4}_{-0.3}$	$1.6^{+0.4}_{-0.6}$
Normalization $K_1$ <sup>a</sup>	$1.2^{+0.2}_{-0.2}$	$2.3^{+0.4}_{-0.5}$	$28^{+1600}_{-28}$	$2.3^{+0.4}_{-0.5}$	$12^{+11}_{-11}$
$T_{e2}$ (MK)				$58^{+690}_{-41}$	$6.3^{+1.0}_{-1.4}$
Normalization $K_2$				$1.1^{+1.5}_{-0.7}$	$1.0^{+2.5}_{-0.7}$
$L_X/10^{37} \text{ erg s}^{-1}$	$2.0^{+0.2}_{-0.2}$	$2.0^{+0.3}_{-0.3}$	$2.0^{+0.7}_{-1.2}$	$2.2^{+0.3}_{-0.3}$	$2.1^{+0.7}_{-0.8}$
$L_X^{int}/10^{37} \text{ erg s}^{-1}$	2.3	4.2	43.7	2.7	12.1
C-stat/bin	167/108	166/108	154/108	145/108	144/108
Derived Parameters <sup>b</sup>					
$V$ [ $f$ ] ( $10^{63} \text{ cm}^3$ )	2.0	2.0	2.0	2.0	2.0
$n_e$ [ $f^{-1/2}$ ] ( $\text{cm}^{-3}$ )	0.03	0.04	0.13	0.54,0.02	0.13,0.03
$P/k$ [ $f^{-1/2}$ ] ( $10^5 \text{ K cm}^{-3}$ )	1.8	2.2	5.5	28	4.2
$M_x$ [ $f^{+1/2}$ ] ( $10^5 M_{\odot}$ )	0.6	0.8	3.1	1.3	3.5
$E_{th}$ [ $f^{+1/2}$ ] ( $10^{53} \text{ erg}$ )	0.7	0.9	2.3	2.7	3.4
$t_c$ [ $f^{+1/2}$ ] (Myr)	40	21	2.5	90	6.2

<sup>a</sup>  $K = (10^{-9}/4\pi D^2) \int n_e n_p dV$

<sup>b</sup> volume filling factor scaling in [ ] in Column 1.

TABLE 12  
INTERMEDIATE AGE REGIONS X-RAY FITTING PARAMETERS

Fit Parameters	apec	apec	apec
$N_{\text{H}}$ ( $10^{21} \text{ cm}^{-2}$ )	0.4	1.1	$0.4^{+5.1}_{-0.0}$
$T_{e1}$ (MK)	$3.1^{+0.3}_{-0.4}$	$3.0^{+0.5}_{-0.5}$	$3.1^{+0.5}_{-1.5}$
Normalization $K_1$ <sup>a</sup>	$0.6^{+0.2}_{-0.2}$	$1.0^{+0.3}_{-0.2}$	$0.6^{+5.1}_{-0.1}$
$L_X/10^{37} \text{ erg s}^{-1}$	$1.0^{+0.1}_{-0.2}$	$1.0^{+0.2}_{-0.2}$	$1.0^{+0.3}_{-0.6}$
$L_X^{int}/10^{37} \text{ erg s}^{-1}$	1.2	1.8	1.2
C-stat/bin	98.5/108	98.7/108	98.5/108
Derived Parameters <sup>b</sup>			
$V$ [ $f$ ] ( $10^{63} \text{ cm}^3$ )	4.0	4.0	4.0
$n_e$ [ $f^{-1/2}$ ] ( $\text{cm}^{-3}$ )	0.01	0.02	0.01
$P/k$ [ $f^{-1/2}$ ] ( $10^5 \text{ K cm}^{-3}$ )	0.8	1.0	0.8
$M_x$ [ $f^{+1/2}$ ] ( $10^5 M_{\odot}$ )	0.6	0.8	0.6
$E_{th}$ [ $f^{+1/2}$ ] ( $10^{53} \text{ erg}$ )	0.7	0.9	0.7
$t_c$ [ $f^{+1/2}$ ] (Myr)	60	50	60

<sup>a</sup>  $K = (10^{-9}/4\pi D^2) \int n_e n_p dV$

<sup>b</sup> volume filling factor scaling in [ ] in Column 1.

with 0.5–2.0 keV luminosities in the range spanned by our sample of star-forming regions and within the central 2/5 radius disk of NGC 2403. Scaling this to the total area occupied by the star-forming regions results in an expected 1.7 X-ray point sources in this luminosity range somewhere within our sample. (Of course, the brighter the point source, the lower the probability of coincidence since the XLF scales as  $L^{-0.58}$ .)

### 3.5. Comparison to Theoretical Expectations

Stellar winds and supernovae within a young star cluster create a hot low-density cavity in the interstellar medium (ISM) which persists beyond the  $\sim 40$  Myr lifetimes of the OB stars in the cluster. The cumulative effect of winds and individual SNe is to gradually sweep the ISM into a thin dense shell analogous to the shell around a stellar wind bubble. The simple physical model of a stellar wind bubble (Castor et al. 1975; Weaver et al. 1977) can be taken over directly to describe, qualitatively, these large HII regions or superbubbles associated with OB associations (McCray & Kafatos 1987; Mac Low & McCray 1988). In this model, massive stars inject kinetic energy into their surroundings creat-

ing a freely expanding wind. Hot shocked gas surrounds this free wind region and occupies most of the volume of the bubble. Surrounding this hot gas is the dense cold swept-up shell. Beyond the shell is the ambient interstellar medium. Diffuse X-ray emission from star-forming regions arises from the tenuous shocked gas in the bubble interior and from higher density gas evaporated from the shell. The dense evaporated component may dominate the X-ray emission which scales as the square of the density.

Although analytic versions of the original basic model have been applied widely in the literature, we note that numerous simplifying assumptions are made which may be poor approximations in reality. Among these are spherical symmetry, constant energy injection rate, adiabaticity, neglect of magnetic fields and of turbulence, and a homogeneous ambient medium. For our present purposes, the most critical of these is the assumption of a constant energy injection rate or mechanical luminosity,  $L_w$ . Numerical simulations (e.g., Strickland & Stevens 1999) show that the expected X-ray luminosity is roughly proportional to  $L_w$  and that  $L_w$  is far from constant.

The starburst synthesis models we have used here (Leitherer & Heckman 1995) show that  $L_w$  (injected by winds from stars of initial mass  $> 15 M_{\odot}$  and by suitably time-averaged SN explosions) is a function of the age of the star-forming region, the mass of the star cluster, and the assumed IMF. Specifically, only stellar winds from massive stars contributes to the mechanical luminosity during the first 3 Myrs. Then supernova explosions begin to contribute resulting in an increase in  $L_w$  by about a factor of 4 from an age of 3 to 6 Myrs. The luminosity decreases again as the contribution from stellar winds declines due to the decreasing number of O stars. From  $\sim 10$  Myrs and up to the last supernova, which is around 40 Myrs,  $L_w$  is almost constant then finally falls quickly to very low values. The young and intermediate star-forming regions studied here have ages in the range where  $L_w$  changes significantly on short timescales so that our estimates of  $L_w$  (Table 10) are reliable only to about a factor of four.

Figure 14 displays the (extinction-corrected) X-ray lu-

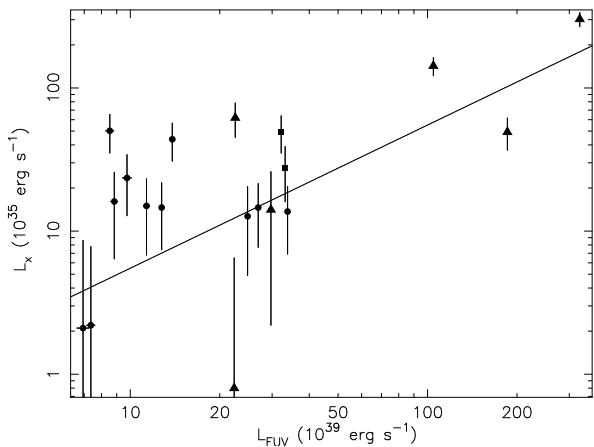


FIG. 11.—  $L_{\text{FUV}}$  vs.  $L_{\text{X}}$  for the 19 star-forming regions. Luminosities are corrected for intrinsic and Galactic extinction. Triangles represent young (less than 2 Myrs), circles intermediate (2–20 Myes), and squares old (above 20 Myrs) star-forming regions. The straight line indicates the best-fitting linear function with a slope of  $(5.5 \pm 0.8) \times 10^{-5}$ .

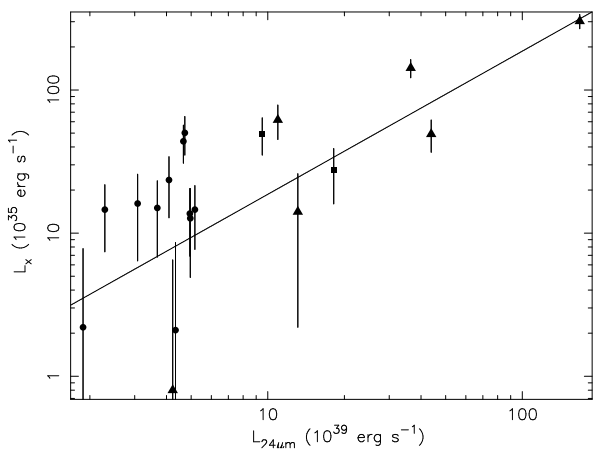


FIG. 12.—  $L_{24\mu\text{m}}$  vs.  $L_{\text{X}}$  for the 19 star-forming regions. Luminosities are corrected for intrinsic and Galactic extinction. Symbols are the same as in Figure 11. The straight line indicates the best-fitting linear function with a slope of  $(1.9 \pm 0.2) \times 10^{-4}$ .

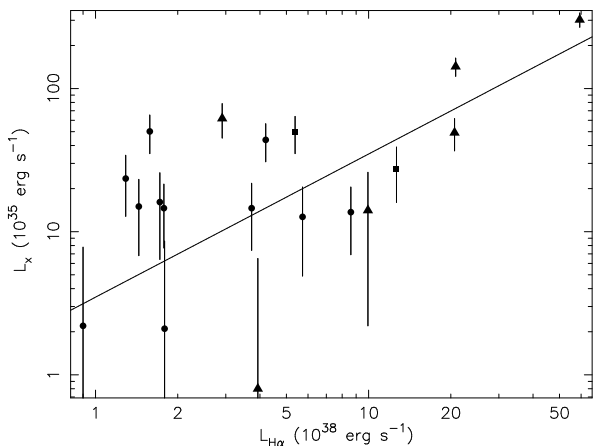


FIG. 13.—  $L_{\text{H}\alpha}$  vs.  $L_{\text{X}}$  for the 19 star-forming regions. Luminosities are corrected for intrinsic and Galactic extinction. Symbols are the same as in Figure 11. The straight line indicates the best-fitting linear function with a slope of  $(3.5 \pm 0.5) \times 10^{-3}$ .

minosity estimated in §3.4 against the mechanical luminosity computed from the (Leitherer & Heckman 1995) models using the age and mass estimates of the star-forming regions deduced in §3.3 (Table 10). Filled triangles depict young regions, and filled circles represent intermediate-age regions. We fitted with linear function for each group, and obtained the slope  $L_{\text{X}}/L_{\text{w}}$ . The resulting slopes are  $0.0033 \pm 0.0005$  for the young regions, and  $0.0017 \pm 0.0005$  for the intermediate-age regions. This is consistent with the *Chandra* result of the second brightest HII region in the local group, NGC 604, whose  $L_{\text{X}}/L_{\text{w}}$  is estimated as 0.002 (Tüllmann et al. 2008).

Numerical simulations (Strickland & Stevens 1999) found that  $L_{\text{X}}/L_{\text{w}}$  for a thin galactic disk model is 0.5–2%, using an  $L_{\text{X}}$  appropriate for the *ROSAT* band. This must be adjusted for the different sensitivity of *Chandra* compared to *ROSAT* for the observed spectral shape. Here, the characteristic electron temperature is 2–3 MK so that the fraction of the luminosity for *Chandra* band (0.5–2.0 keV) to *ROSAT* band (0.1–2.5 keV) is 0.5 to 0.6. This translates  $L_{\text{X}}/L_{\text{w}}$  to 0.25 to 1% for the *Chandra* band which is consistent with our results.

Figure 15 displays the (extinction-corrected) X-ray emission against the estimated cluster age. Here, the X-ray luminosities are scaled to a fixed cluster mass of  $10^5 M_{\odot}$  for easy comparison to  $L_{\text{w}}(t)$ . The solid curve represents the best-fitting scaling,  $L_{\text{X}} = 0.0017 L_{\text{w}}$ , from Figure 14 for the intermediate-age clusters and the dashed line is the factor-of-two higher scaling appropriate for the younger clusters. Note the roughly factor-of-four change in  $L_{\text{w}}$  at  $t \sim 4$  Myr as described above. Unfortunately, there is a considerable amount of scatter among the individual regions. For this reason, the  $L_{\text{X}}/L_{\text{w}}$  ratio is not a sensitive independent measure of the age of a cluster.

#### 4. DISCUSSION OF INDIVIDUAL STAR-FORMING REGIONS

We have examined 19 star-forming regions in the central part of NGC 2403. Their basic properties are listed in Tables 9 and 10. They range in age from 1 to 16 Myr with two much older regions at 50 and 60 Myr. These latter ages are likely poor estimates as these two regions are also strong  $\text{H}\alpha$  sources which argues against an old age. The remaining star-forming regions fall into distinct age groups; young (1–3 Myr) and intermediate (7 to 16 Myr). The bulk X-ray properties of the hot gas within these two age groups, from model fits to their stacked X-ray spectra, are summarized in Tables 11 and 12, respectively.

There is very little change in the X-ray temperatures and very little change in the X-ray luminosity per unit star cluster mass with age (Figure 15). There is also no significant evolution in the ratio of the X-ray luminosity to the mechanical luminosity (Figure 14). Thus, the basic X-ray observables, temperature and luminosity, do not trace evolutionary changes for this sample of young star-forming regions.

However, the density of the hot gas derived from the spectral fitting and hence the gas pressure in the young star clusters is about a factor of 2 higher than in the intermediate age clusters. This is consistent with the trends deduced previously (§2) where the youngest sources, the

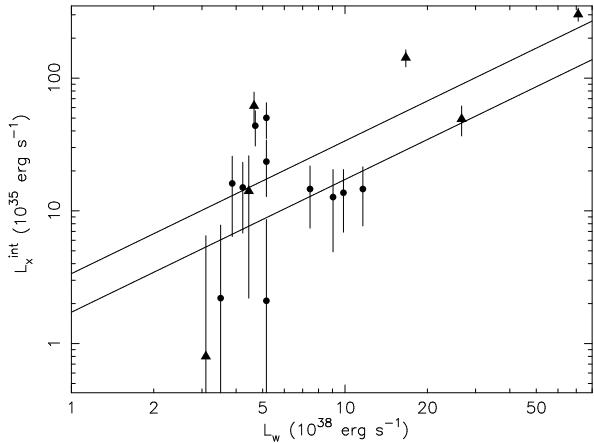


FIG. 14.— Mechanical luminosity,  $L_w$  calculated from Starburst99 scaled by the mass and age of each region is shown against the intrinsic X-ray luminosity. Symbols are the same as in Figure 11 (the two regions older than 20 Myr are omitted because they have very low mechanical luminosities according to Starburst99). The lines indicate best-fitting slopes of  $(3.4 \pm 0.5) \times 10^{-3}$  and  $(1.7 \pm 0.5) \times 10^{-3}$  fitted to the young and intermediate-age regions, respectively.

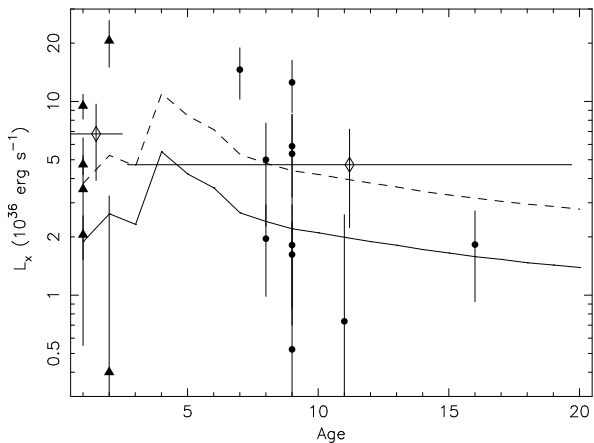


FIG. 15.— Intrinsic X-ray luminosity is shown against age of star forming regions. Luminosities are scaled to an initial mass of  $10^5 M_\odot$ . Symbols are the same as in Figure 11. Open diamonds depict the average for young and intermediate regions. The solid curve indicates the X-ray luminosity scaled from the mechanical luminosity,  $L_w$ , assuming  $L_X/L_w = 0.0017$ . The dashed curve indicates the X-ray luminosity scaled from  $L_w$  assuming  $L_X/L_w = 0.0034$ .

SNRs, have the highest densities and pressures followed by the (H $\alpha$ -selected) HII regions with the residual X-ray emission having the lowest density and pressure.

There are three plausible scenarios for the nature of the hot residual gas consistent with these observed trends. (1) If the decrease in density is temporal, then the residual emission comes from gas initially heated at times considerably more than  $\sim 20$  Myr in the past (the age of the intermediate group of star-forming regions); i.e., it is a relic of past star-formation activity. This is consistent with the absence of a spatial correlation between tracers of recent star formation and this residual emission. (2) The hot residual gas may be escaping from active star-forming regions into lower-density voids in the disk

ISM. These low-density voids may be, for instance, localized remnants of past star-forming activity. If this were the case, then we would expect some of this hot gas to be surrounding the star-forming regions analyzed here. We checked this possibility by taking successively larger X-ray source sizes for the 19 star-forming regions to estimate the true source extent. We found that for sizes up to twice the values adopted above (which were the maximum radii estimated from the UV and mid-IR images) there is a clear net X-ray excess (above the background). Nevertheless, on larger scales, the morphology of the residual hot gas does not correlate well with the star-formation tracers. (3) The hot residual gas may have moved out of the plane of the galaxy down the density gradient into the halo. However, again, as there is no evidence from the distribution of the residual gas that strongly correlates it with star-forming regions, it must be a relic of past activity. In fact, there are no regions of active star formation that have the signature of blowout from the disk. Blowout requires that the bubble size be roughly a few times the density scale height. The largest star-forming regions in the central regions of NGC 2403 are  $\sim 200$  pc compared to a canonical scale height for late-type spirals of 250–500 pc (see also the discussion in Strickland et al. 2004).

We note that the age of the hot residual gas inferred from all of these scenarios is roughly the same as the timescale for gravitational instabilities to cause shells surrounding OB associations to fragment (McCray & Kafatos 1987) at which point hot gas can vent out into the surroundings. It is also an age at which strong ionizing continua from massive stars has ended though SNe may still be active. The current cooling time for the residual gas exceeds 20 Myr and may be as high as 340 Myrs. Thus, regardless of the actual location of the residual gas (disk or halo) and the time elapsed since it formed ( $< 10$ – $20$  Myr if escaping from active star-forming regions or perhaps factors of a few longer if remnants of past activity), this gas is likely to continue to radiate at low levels for a time longer than the characteristic timescales for localized star formation.

## 5. SUMMARY

We have revisited the study of the current and recent star formation activity in the central regions of normal late-type spiral galaxy NGC 2403 by re-evaluating the existing X-ray data and including supporting observations at other key wavebands. These include *Spitzer* images that trace dust heated by massive stars, *GALEX* images showing the young stars, and H $\alpha$  observations that reveal nebulae photoionized by massive stars and SNe. Through analysis of this multi-wavelength data, we have obtained estimates of the mass, age, and line-of-sight extinction towards numerous young star clusters. With few exceptions, these clusters and their environs are weak X-ray sources. Even the most powerful, a giant HII region comparable to 30 Dor in the LMC and NGC 604 in M33, radiates at only  $\sim 3 \times 10^{37}$  erg s $^{-1}$  in the *Chandra* X-ray band which is about 0.5% of its estimated mechanical luminosity.

We have also shown that, after carefully accounting for the point-source (X-ray binary) population, SNRs and bright HII regions, there remains a residual X-ray component pervading the central few kpc of NGC 2403. This

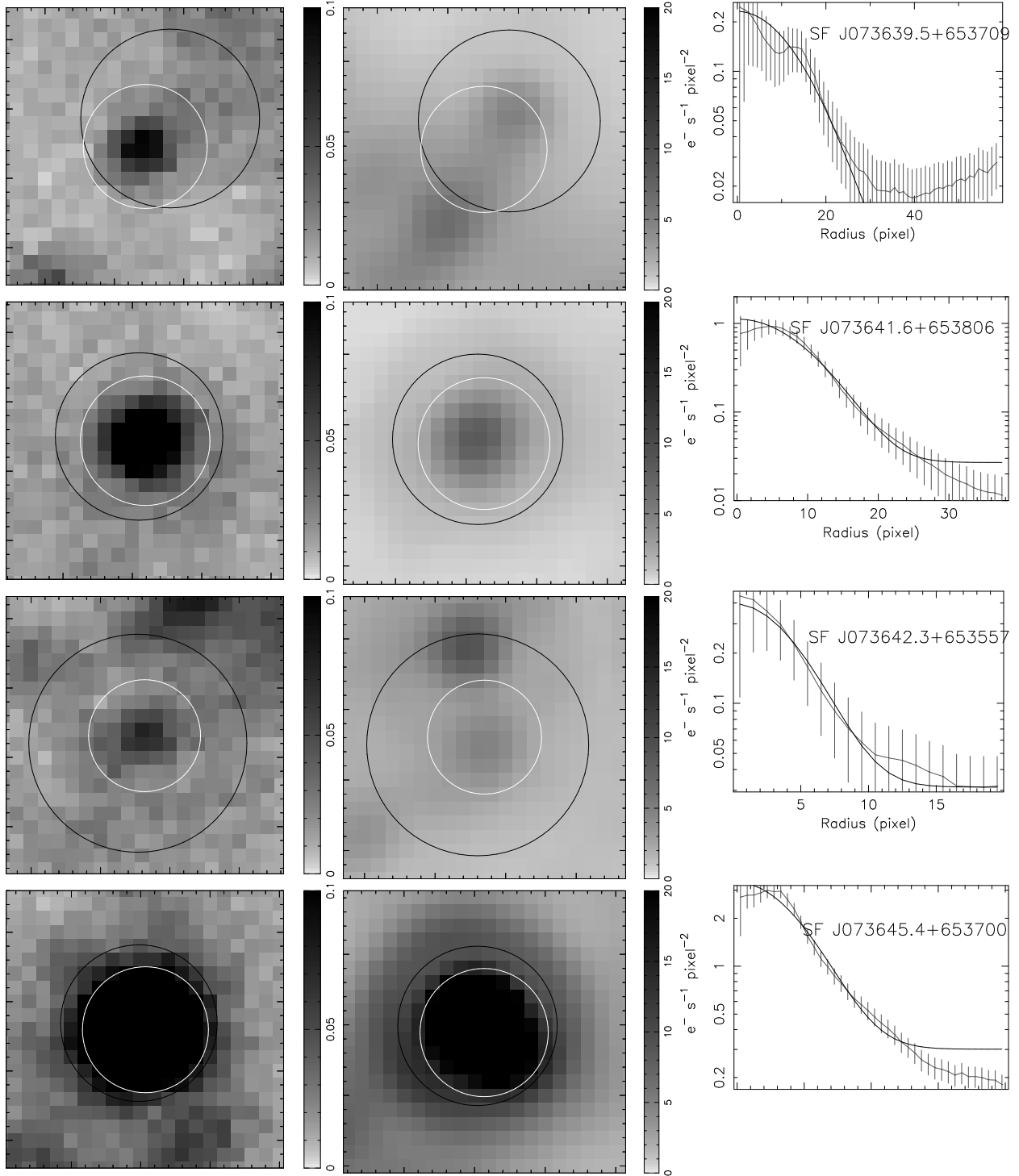
component cannot be accounted for by faint sources below our detection limit. It is likely diffuse hot gas but not strongly correlated with current star-formation activity. It is likely a relic of star formation activity occurring some 20 Myrs (the age of the intermediate age regions) or older.

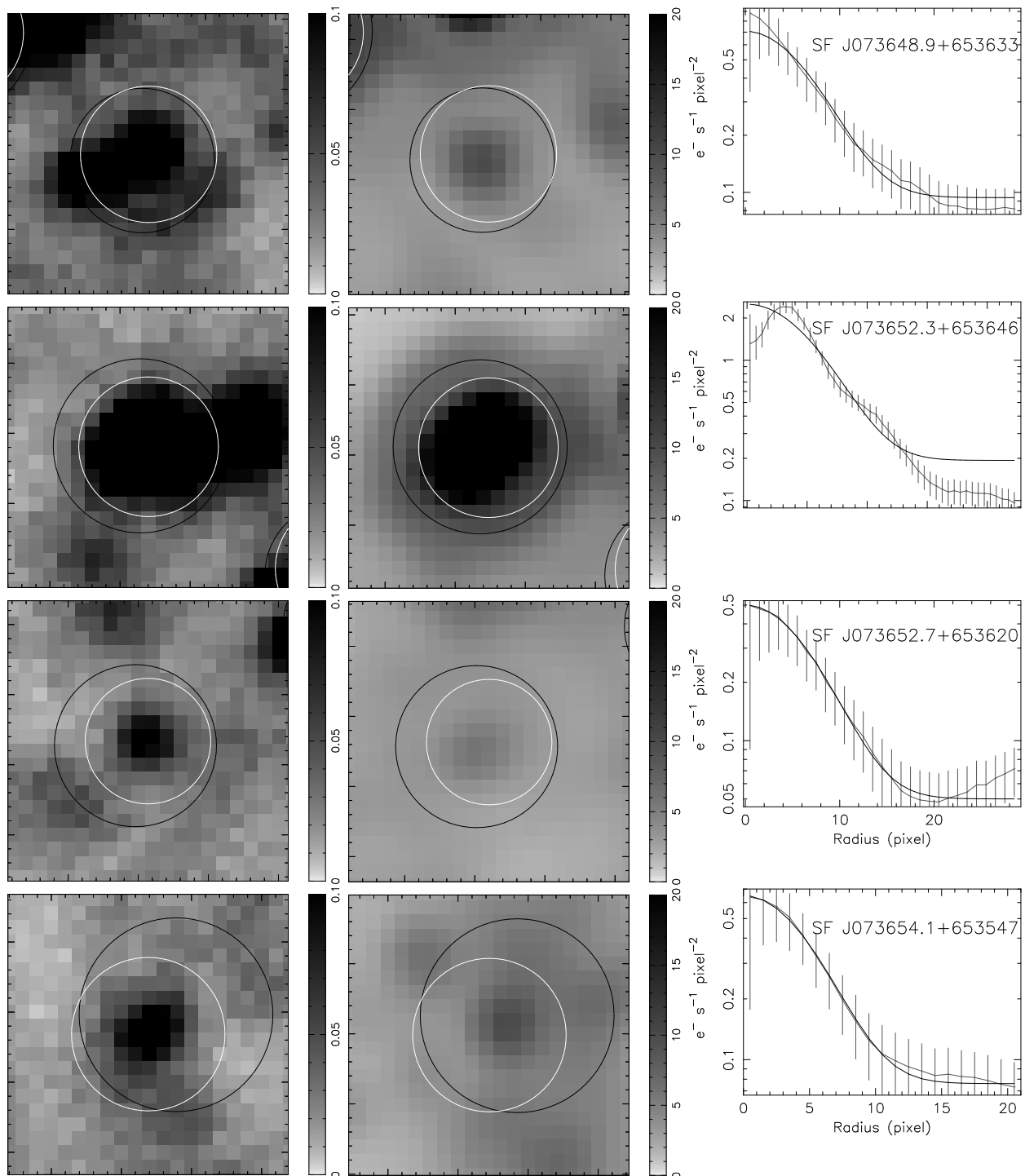
The geometry of the residual hot gas is not well determined, which leads to additional uncertainties in its physical properties. It is not clear whether this gas is confined to the disk of the galaxy or resides in the halo. Nonetheless, it seems to be more centrally-located than the star-forming regions. Since the amount of hot gas represented by this residual emission is substantial, it implies that star-formation activity was much higher in the past. Combined with its central location, this conclusion is consistent with the suggestion by Davidge & Courteau (2002) who suggested that an earlier episode of star formation occurred in the central region of NGC 2403 that has now propagated outward in the disk to its present radius of about a kpc from the galactic center.

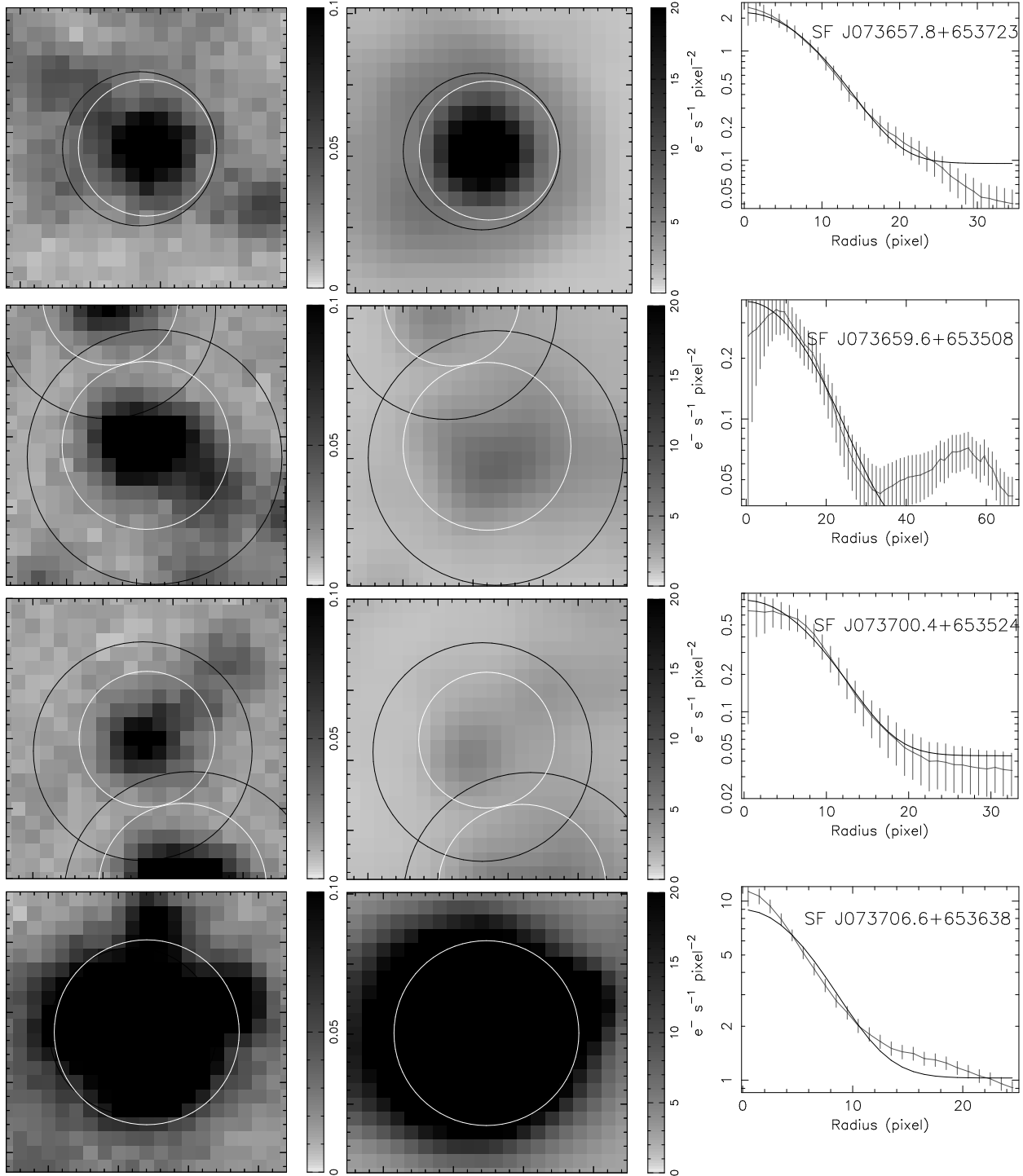
We gratefully acknowledge the anonymous referee for careful reading and insightful comments that improved the paper. Support for this research was provided in part by NASA through an Astrophysics Data Analysis Program grant NNX08AJ49G and through the NASA/*Chandra* Award Number GO5-6089A issued by the *Chandra* X-ray Observatory Center, which is operated by the Smithsonian Astrophysical Observatory for and on behalf of NASA under contract NAS8-03060. This work made use of observations made with the *Chandra*; of observations made with the Spitzer Space Telescope, which is operated by the Jet Propulsion Laboratory, California Institute of Technology, under a contract with NASA; of observations made with the Galaxy Evolution Explorer, a NASA mission managed by the Jet Propulsion Laboratory; and of ground-based observations obtained as part of the Spitzer Legacy Science project SINGS (Kennicutt et al. 2003) to which we are greatly indebted.

#### REFERENCES

- Anders, E., & Grevesse, N. 1989, *Geochim. Cosmochim. Acta*, 53, 197
- Argo, M. K., Muxlow, T. W. B., Beswick, R. J., Pedlar, A., & Marcaide, J. M. 2004, *IAU Circ.*, 8399, 3
- Barnes, J. E., & Hernquist, L. 1992, *ARA&A*, 30, 705
- Böker, T., Laine, S., van der Marel, R. P., Sarzi, M., Rix, H.-W., Ho, L. C., & Shields, J. C. 2002, *AJ*, 123, 1389
- Bregman, J. N. 1980, *ApJ*, 236, 577
- Calzetti, D. 2001, *PASP*, 113, 1449
- Calzetti, D., et al. 2005, *ApJ*, 633, 871
- Cardelli, J. A., Clayton, G. C., & Mathis, J. S. 1989, *ApJ*, 345, 245
- Castor, J., McCray, R., & Weaver, R. 1975, *ApJ*, 200, L107
- Cole, S., Lacey, C. G., Baugh, C. M., & Frenk, C. S. 2000, *MNRAS*, 319, 168
- Davidge, T. J., & Courteau, S. 2002, *AJ*, 123, 1438
- Drissen, L., Roy, J.-R., Moffat, A. F. J., & Shara, M. M. 1999, *AJ*, 117, 1249
- Fraternali, F., & Binney, J. J. 2006, *MNRAS*, 366, 449
- . 2008, *MNRAS*, 386, 935
- Fraternali, F., Cappi, M., Sancisi, R., & Oosterloo, T. 2002a, *ApJ*, 578, 109
- Fraternali, F., Oosterloo, T., & Sancisi, R. 2004, *A&A*, 424, 485
- Fraternali, F., van Moorsel, G., Sancisi, R., & Oosterloo, T. 2002b, *AJ*, 123, 3124
- Garnett, D. R., Shields, G. A., Peimbert, M., Torres-Peimbert, S., Skillman, E. D., Dufour, R. J., Terlevich, E., & Terlevich, R. J. 1999, *ApJ*, 513, 168
- Garnett, D. R., Shields, G. A., Skillman, E. D., Sagan, S. P., & Dufour, R. J. 1997, *ApJ*, 489, 63
- Gil de Paz, A., et al. 2007, *ApJS*, 173, 185
- Heckman, T. M., Kauffmann, G., Brinchmann, J., Charlot, S., Tremonti, C., & White, S. D. M. 2004, *ApJ*, 613, 109
- Karachentsev, I. D., Karachentseva, V. E., Huchtmeier, W. K., & Makarov, D. I. 2004, *AJ*, 127, 2031
- Karachentsev, I. D., et al. 2002, *A&A*, 383, 125
- Kennicutt, Jr., R. C. 1989, *ApJ*, 344, 685
- Kennicutt, Jr., R. C., et al. 2003, *PASP*, 115, 928
- Kent, S. M. 1987, *AJ*, 93, 816
- Kormendy, J., & Kennicutt, Jr., R. C. 2004, *ARA&A*, 42, 603
- Kroupa, P. 2001, *MNRAS*, 322, 231
- Leitherer, C., & Heckman, T. M. 1995, *ApJS*, 96, 9
- Leitherer, C., et al. 1999, *ApJS*, 123, 3
- Mac Low, M.-M., & McCray, R. 1988, *ApJ*, 324, 776
- Madore, B. F., & Freedman, W. L. 1991, *PASP*, 103, 933
- Martin, C. L., & Kennicutt, Jr., R. C. 2001, *ApJ*, 555, 301
- Martin, P., & Belley, J. 1996, *ApJ*, 468, 598
- Matonick, D. M., Fesen, R. A., Blair, W. P., & Long, K. S. 1997, *ApJS*, 113, 333
- McCray, R., & Kafatos, M. 1987, *ApJ*, 317, 190
- Moretti, A., Campana, S., Lazzati, D., & Tagliaferri, G. 2003, *ApJ*, 588, 696
- Noguchi, M. 2000, *MNRAS*, 312, 194
- Pannuti, T. G., Schlegel, E. M., & Lacey, C. K. 2007, *AJ*, 133, 1361
- Pérez-González, P. G., et al. 2006, *ApJ*, 648, 987
- Prescott, M. K. M., et al. 2007, *ApJ*, 668, 182
- Schaap, W. E., Sancisi, R., & Swaters, R. A. 2000, *A&A*, 356, L49
- Schlegel, D. J., Finkbeiner, D. P., & Davis, M. 1998, *ApJ*, 500, 525
- Schlegel, E. M., & Pannuti, T. G. 2003, *AJ*, 125, 3025
- Shapiro, P. R., & Field, G. B. 1976, *ApJ*, 205, 762
- Sheth, K., Vogel, S. N., Regan, M. W., Thornley, M. D., & Teuben, P. J. 2005, *ApJ*, 632, 217
- Sicking, F. J. 1997, PhD thesis, PhD Thesis, University of Groningen, (1997)
- Sivan, J.-P., Maucherat, A. J., Petit, H., & Comte, G. 1990, *A&A*, 237, 23
- Spitzer, L. J. 1990, *ARA&A*, 28, 71
- Strickland, D. K., Heckman, T. M., Colbert, E. J. M., Hoopes, C. G., & Weaver, K. A. 2004, *ApJ*, 606, 829
- Strickland, D. K., & Stevens, I. R. 1999, *MNRAS*, 306, 43
- Struck, C., & Smith, D. C. 2009, *MNRAS*, 1189
- Tennant, A. F. 2006, *AJ*, 132, 1372
- Thornley, M. D., & Wilson, C. D. 1995, *ApJ*, 447, 616
- Tüllmann, R., et al. 2008, *ApJ*, 685, 919
- Vázquez, G. A., & Leitherer, C. 2005, *ApJ*, 621, 695
- Weaver, R., McCray, R., Castor, J., Shapiro, P., & Moore, R. 1977, *ApJ*, 218, 377
- Yukita, M., Swartz, D. A., Soria, R., & Tennant, A. F. 2007, *ApJ*, 664, 277









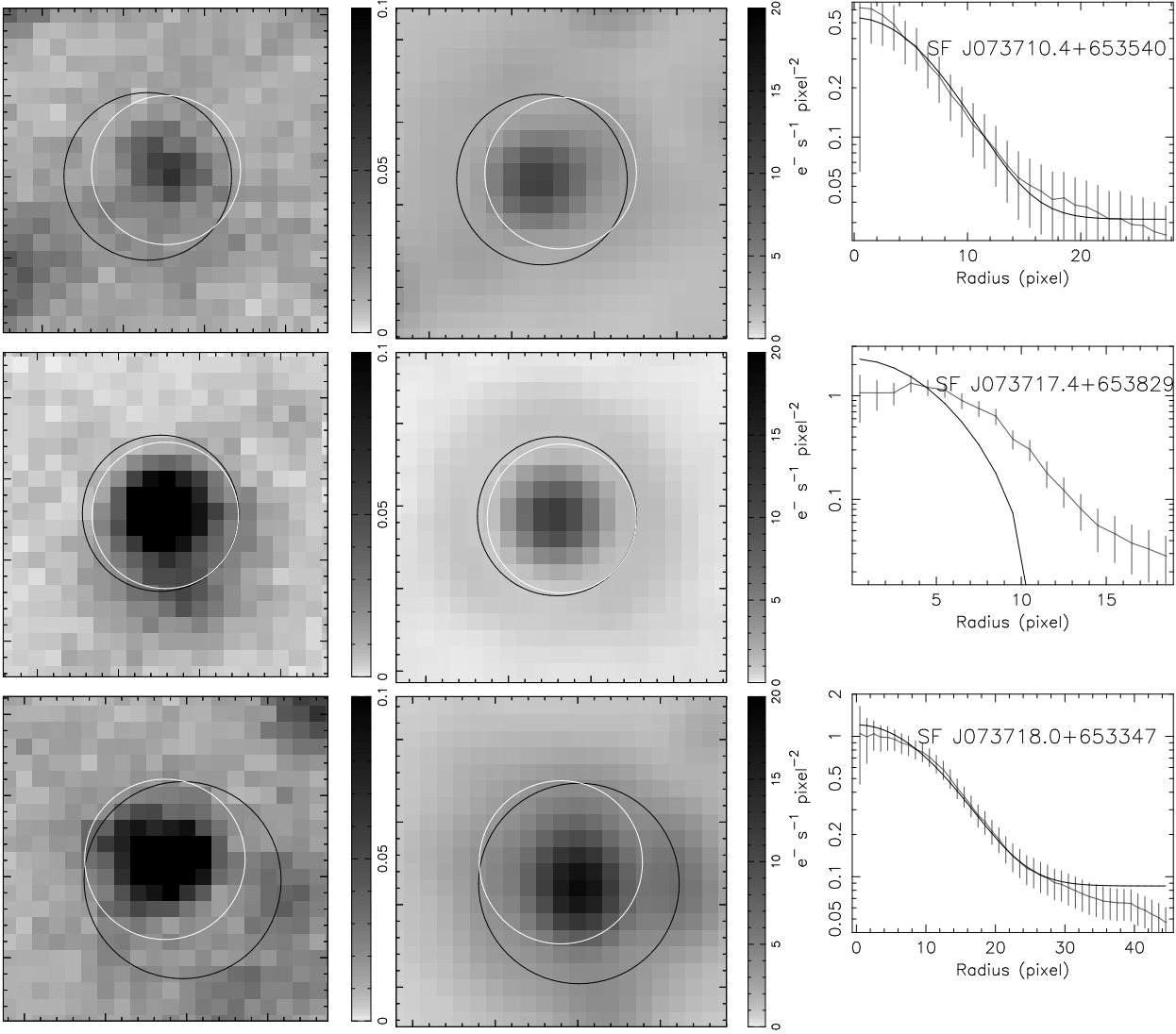


FIG. 8 CONT.—  $30'' \times 30''$  close-up views of the rest 15 of 19 star-forming regions. FUV images are on the left and  $24\ \mu\text{m}$  images are in the middle. Circle locations, sizes, colors, and gray scales are the same as in Figure 7. On the right are higher-resolution  $\text{H}\alpha$  radial profiles shown with best-fitting Gaussian model curves. Each radial profile extends to 5 Gaussian widths. One pixel corresponds to  $0.''304$ .